# Diagnosing quantum phases using long-range two-site quantum resource behavior

Lin-Lin Su,[1,2] Jun Ren,[1,3,*] Wen-Long Ma,[2,4,†] Z. D. Wang,[3,5,‡] and Yan-Kui Bai[1,3,§]
[1]*College of Physics and Hebei Key Laboratory of Photophysics Research and Application, Hebei Normal University, Shijiazhuang, Hebei 050024, China*
[2]*State Key Laboratory of Superlattices and Microstructures, Institute of Semiconductors, Chinese Academy of Sciences, Beijing 100083, China*
[3]*Department of Physics, HK Institute of Quantum Science & Technology, and Guangdong-Hong Kong Joint Laboratory of Quantum Matter, The University of Hong Kong, Pokfulam Road, Hong Kong, China*
[4]*Center of Materials Science and Opto-Electronic Technology, University of Chinese Academy of Sciences, Beijing 100049, China*
[5]*Quantum Science Center of Guangdong-Hong Kong-Macau Great Bay Area, 3 Binlang Road, Shenzhen 518045, China*

(Received 13 November 2023; revised 14 July 2024; accepted 17 August 2024; published 3 September 2024)

We propose and demonstrate that the behaviors of long-range, two-site quantum resources can effectively diagnose quantum phases. In an XX spin chain with symmetry-breaking quantum phase transitions, we reveal that the gradually decaying and damped oscillating modes of quantum coherence or quantum discord, along with two-site distance, can identify two spin-liquid phases, respectively. Moreover, based on our analytical results of spin correlation functions, we confirm the existence of long-range entanglement in the system and establish a connection between two-site entanglement and quantum phases. Furthermore, for the extended Ising model with topological phase transitions, we find that coherence and quantum discord behaviors can also signify topological quantum phases. In particular, we discover the quantum resource freezing phenomenon, where topologically protected long-range quantum resources may have potential applications in quantum information processing.

DOI: 10.1103/PhysRevB.110.104101

## I. INTRODUCTION

Quantum resources [1], including quantum coherence, entanglement, and quantum discord, are fundamental to numerous quantum information processing (QIP) tasks [2–5]. Simultaneously, they have been developed into a powerful tool for studying physical properties in quantum many-body systems, with the relationship between quantum resources and quantum phases being a particularly fascinating problem [6–9].

Quantum phase transitions (QPTs) in many-body systems are accompanied by dramatic changes in their physical properties [10], often exhibiting distinguishable signatures on quantum resources. In a piece of pioneering work, Osterloh *et al.* revealed the scaling behavior of two-site entanglement [11] near the QPT point in the transverse Ising model [12]. Beyond short-range, two-site entanglement, other long-range quantum resources such as quantum coherence [13–18], quantum discord [19,20], and multipartite entanglement [21–28] can also characterize various spin models exhibiting symmetry-breaking QPTs [29–41], as well as topological quantum phase transitions (TQPTs) described by symmetry-protected topological order [42–54].

Although characterizing QPTs based on quantum resources has achieved significant success in the last couple of decades, identifying different quantum phases in many-body systems remains challenging [55–57]. Recently, it was demonstrated that multipartite entanglement, evidenced by the scaling behavior of quantum Fisher information (QFI) [58–61], can characterize symmetry-protected topological phases in an extended Kitaev chain [55,56]. However, it is both experimentally challenging to detect the QFI for a large system and to extract the scaling exponents by tuning the spin chain length [62–64]. While it is believed that two-site quantum resources are more easily accessed experimentally than the QFI [62] since they can be expressed as the functions of two-spin correlations in general [65–68], it remains unexplored whether the behaviors of two-site quantum resources can diagnose different quantum phases in many-body systems.

In this paper, we study the behaviors of long-range two-site quantum resources and reveal that the decay modes of these resources, along with two-site distance, can indeed diagnose quantum phases in many-body systems. In an XX chain with three-spin interactions [32] exhibiting symmetry-breaking QPTs, we show that the gradually decaying and damped oscillating modes of two-site quantum coherence and quantum correlations [19,20] can identify two types of spin-liquid phases. The behavior of long-range two-site entanglement [11] confirmed by our analytical results exhibits the same functionality. Furthermore, in the extended Ising model with TQPTs [51], we examine the relationship between two-site quantum resources and topological quantum phases, and discover a quantum resource freezing phenomenon that

*Contact author: renjun@hebtu.edu.cn
†Contact author: wenlongma@semi.ac.cn
‡Contact author: zwang@hku.hk
§Contact author: ykbai@semi.ac.cn

 

can characterize the topological quantum phases with winding numbers $\mathcal{N} = \pm 1$.

## II. EXTENDED ISING MODEL AND ITS TWO-SITE QUANTUM STATES

We study the extended Ising model with three-spin interactions [51],

$$H = -\sum_{j=1}^{L}\Big[\frac{1+\gamma}{2}\sigma_j^x\sigma_{j+1}^x + \frac{1-\gamma}{2}\sigma_j^y\sigma_{j+1}^y + \lambda\sigma_j^z + \alpha\sigma_j^z\Big(\frac{1+\delta}{2}\sigma_{j-1}^x\sigma_{j+1}^x + \frac{1-\delta}{2}\sigma_{j-1}^y\sigma_{j+1}^y\Big)\Big], \quad (1)$$

where $L$ is total spin number in the spin chain, $\gamma$ is the anisotropic parameter of the nearest-neighbor couplings, $\lambda$ is the strength of external magnetic field, $\alpha$ and $\delta$ represent the strength and anisotropy of three-spin interactions, and $\sigma_j^x$, $\sigma_j^y$, and $\sigma_j^z$ are the Pauli operators on the $j$th spin. When $\gamma = \delta = 0$, the system is the XXT model (an XX chain with isotropic three-spin interactions) exhibiting the symmetry-breaking QPTs. In a generic case for $\gamma \neq 0$ and $\delta \neq 0$, the extended Ising model exhibits the topological QPTs.

The Hamiltonian in Eq. (1) can be exactly diagonalized and a review on the details is presented in Appendix A. For the $i$th and $j$th spins, the two-site reduced density matrix of the ground state has the form

$$\rho_r = \rho_{ij} = \begin{pmatrix} u^+ & 0 & 0 & y^- \\ 0 & z & y^+ & 0 \\ 0 & y^+ & z & 0 \\ y^- & 0 & 0 & u^- \end{pmatrix}, \quad (2)$$

where $r = |j - i|$ denotes the distance between the two spins, and the nonzero matrix elements are $u^{\pm} = (1 \pm 2\langle\sigma^z\rangle + \langle\sigma_0^z\sigma_r^z\rangle)/4$, $z = (1 - \langle\sigma_0^z\sigma_r^z\rangle)/4$, and $y^{\pm} = (\langle\sigma_0^x\sigma_r^x\rangle \pm \langle\sigma_0^y\sigma_r^y\rangle)/4$. The magnetization $\langle\sigma^z\rangle$ and two-site correlations $\langle\sigma_0^s\sigma_r^s\rangle$ with $s = x, y, z$ are the functions of $G_r$ (see the explicit expressions in Appendix B). For a finite chain length $L$ at zero temperature, the $G_r$ function can be written as [69,70]

$$G_r = -\frac{1}{L}\sum_k \frac{1}{\Lambda_k}\{\cos(\phi_k r)z_k + \sin(\phi_k r)y_k\}, \quad (3)$$

where $\phi_k = 2\pi k/L$ with $k = -M, \ldots, M$ and $M = (L-1)/2$ for odd $L$, the energy spectra $\Lambda_k = \sqrt{z_k^2 + y_k^2}$ with $z_k = \lambda - \cos\phi_k - \alpha\cos(2\phi_k)$, and $y_k = \gamma\sin\phi_k + \alpha\delta\sin(2\phi_k)$. In the thermodynamic limit, the function has the integral form [71]

$$G_r = -\frac{1}{\pi}\int_0^{\pi} F(\gamma, \lambda, \alpha, \delta, r)d\phi, \quad (4)$$

where the kernel is $F(\gamma, \lambda, \alpha, \delta, r) = [\cos(\phi r)z + \sin(\phi r)y]/\Lambda_\phi$ with the parameters being $\Lambda_\phi = \sqrt{z^2 + y^2}$, $z = \lambda - \cos\phi - \alpha\cos(2\phi)$, and $y = \gamma\sin\phi + \alpha\delta\sin(2\phi)$. The $G_r$ function here is vital in calculating quantum state $\rho_r$ and analyzing the behaviors of two-site quantum resources.

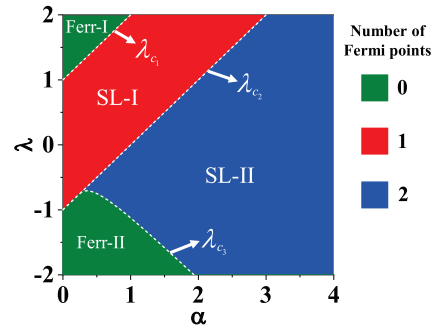


FIG. 1. The ground-state phase diagram of the XXT model described by the number of Fermi points, where there are two Fermi points $\phi_+$ and $\phi_-$ in the SL-II phase (blue region), one point $\phi_+$ in the SL-I phase (red region), and zero in ferromagnetic phase (green regions of Ferr-I and Ferr-II).

## III. CHARACTERIZATION OF QUANTUM PHASES IN THE XXT MODEL

We first consider the XXT model for which the Hamiltonian in Eq. (1) has the parameters $\gamma = 0$ and $\delta = 0$ [32]. In this case, the ground-state phase diagram is composed of ferromagnetic phase, spin-liquid I (SL-I) phase and spin-liquid II (SL-II) phase [72]. The symmetry-breaking QPTs are connected with the number of Fermi points [72–77]. By solving the energy equation $\Lambda_\phi = 0$ with $\phi \in \{0, \pi\}$ in the thermodynamic limit, we obtain the two real Fermi points

$$\phi_{\pm}(\alpha, \lambda) = \arccos\Big[\frac{-1 \pm \sqrt{1 + 8\alpha^2 + 8\alpha\lambda}}{4\alpha}\Big]. \quad (5)$$

As shown in Fig. 1, we find the number of Fermi points can not only detect the QPTs but also identify the three quantum phases, where there are two Fermi points in the SL-II phase, one in the SL-I phase, and zero in ferromagnetic phase (a detailed analysis on the Fermi points is presented in Appendix C). The white dashed lines are critical lines representing phase boundaries with $\lambda_{c_1} = \alpha + 1$, $\lambda_{c_2} = \alpha - 1$, and $\lambda_{c_3} = -(1 + 8\alpha^2)/8\alpha$ ($\alpha \geqslant 0.25$ for $\lambda_{c_3}$).

We now study the property of long-range two-site quantum coherence of reduced state $\rho_r$ along with the distance of two spins in the XXT spin chain. Quantum coherence is an important resource in the QIP [78,79] and quantum thermodynamics [80–83]. Here we adopt the $l_1$-norm quantum coherence [13], which is expressed as the sum of modulus of off-diagonal element: $C_{l_1}(\rho_r) = \sum_{i,j,i\neq j}|\rho_{ij}|$. In the XXT model, since the Hamiltonian is isotropic in the $x$ and $y$ directions ($\gamma = \delta = 0$), we have the matrix element $y^- = (\langle\sigma_0^x\sigma_r^x\rangle - \langle\sigma_0^y\sigma_r^y\rangle)/4 = 0$ in Eq. (2). Therefore, the $l_1$-norm coherence of two-site quantum state is

$$C_{l_1}(\rho_r) = 2|y^+| = \big|\langle\sigma_0^x\sigma_r^x\rangle\big|, \quad (6)$$

where the spin correlation $\langle\sigma_0^x\sigma_r^x\rangle$ is a determinant of $G_r$ matrix (see the details in Appendix D). In order to obtain the quantum coherence expediently, we derive the analytical formula of $G_r$ function in the thermodynamic limit for different

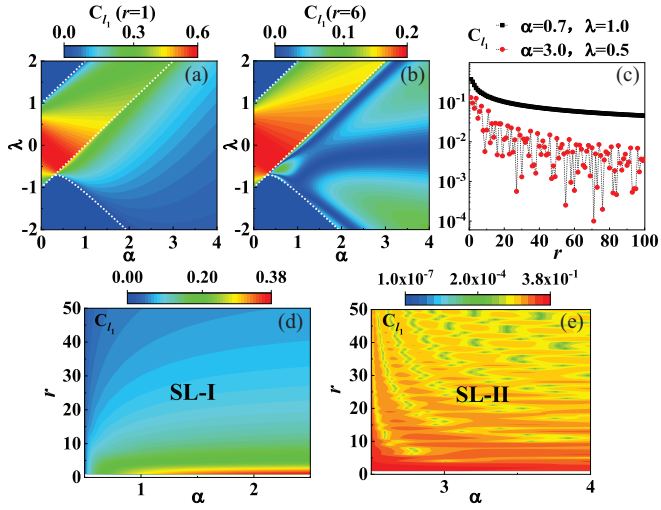


FIG. 2. The $l_1$-norm coherence in the XXT model. $C_{l_1}(\alpha, \lambda)$ for two-site distances: (a) $r = 1$ and (b) $r = 6$ with the white dashed lines being the phase boundaries. In (c), two set parameters are chosen for $C_{l_1}(r)$ in the SL-I and SL-II phases, and the gradually decaying and damped oscillating modes of the coherence along with two-site distance are further illustrated in (d) and (e).

regions of quantum phases

$$G_r = \begin{cases} -\delta_{0r}, & \text{Ferr-I} \\ \delta_{0r}, & \text{Ferr-II} \\ \frac{2\sin(r\phi_+)}{\pi r} - \delta_{0r}, & \text{SL-I} \\ 2\left(\frac{\sin(r\phi_+)}{\pi r} - \frac{\sin(r\phi_-)}{\pi r}\right) + \delta_{0r}, & \text{SL-II} \end{cases} \tag{7}$$

where $r$ is the distance of two spins and $\phi_\pm$ are the Fermi points given in Eq. (5). According to this analytical formula, the spin correlation $\langle \sigma_0^x \sigma_r^x \rangle$ is zero in the ferromagnetic phase, and then the corresponding quantum coherence is $C_{l_1}(\rho_r) = 0$. However, the quantum coherence in the SL-I and SL-II phases is nonzero in general, where we can obtain a closed-form expression in terms of system parameters for each fixed two-site distance $r$ (see the analytical expression in Appendix D). As shown in Figs. 2(a) and 2(b), we plot quantum coherence $C_{l_1}(\rho_r)$ as a function of magnetic field $\lambda$ and interaction strength $\alpha$ for spin-spin distances $r = 1$ and 6. We can distinguish the SL-I and SL-II phases from the ferromagnetic phase with zero coherence, and the change patterns of $C_{l_1}$ are different where $C_{l_1}$ is gradually decaying in SL-I phase and oscillating in SL-II phase. The intrinsic reason is that the coherence decays along with the distance $r$ in the gradually decaying mode for SL-I phase but in the damped oscillating mode for SL-II phase, as shown in Fig. 2(c). Therefore, the gradually decaying and damped oscillating mode of $C_{l_1}$ can serve as an effective diagnostic of quantum phases, as illustrated by Figs. 2(d) and 2(e).

Next, we study two-site quantum entanglement in the same model. As quantified by concurrence [11], the two-site entanglement can be written as

$$C(\rho_r) = \max\{0, 2(|y^+| - \sqrt{u^+ u^-})\}, \tag{8}$$

where $y^+$ and $u^\pm$ are the off-diagonal and diagonal elements of reduced quantum state $\rho_r$ in Eq. (2), respectively. In

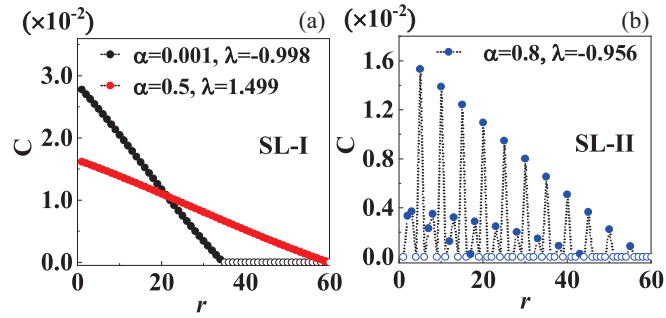


FIG. 3. Long-range two-site entanglement in (a) SL-I phase and (b) SL-II phase, where the concurrence decays in the gradual mode for SL-I phase but in the oscillating mode for SL-II phase. The hollow dots indicate the distances with zero entanglement.

comparison with the $l_1$-norm coherence in Eq. (6), the two-site entanglement is smaller than corresponding quantum coherence. In the previous analysis, we know that the coherence has the long-range property, but whether there exists long-range two-site entanglement is an open problem in multipartite spin systems without long-range interactions [12,40,84–89]. In the XXT model, although the concurrence is short range (no more than the next-nearest neighbor) in generic regions of SL-I and SL-II phases, we confirm the existence of long-range two-site entanglement for which the parameters are close to the phase boundaries (see Fig. 1) described by the critical lines $\lambda_{c_1}$, $\lambda_{c_2}(\alpha \leqslant 0.25)$, and $\lambda_{c_3}$ (a detailed analysis is given in Appendix E). In SL-I and SL-II phases, we choose three sets of parameters near the phase boundaries, and calculate the concurrence as a function of two-site distance. As shown in Fig. 3, the distinct decay modes of long-range two-site entanglement have the same functionality for identifying quantum phases.

## IV. CHARACTERIZATION OF TOPOLOGICAL QUANTUM PHASES IN THE EXTENDED ISING MODEL

In the extended Ising system with $\gamma \neq 0$ and $\delta \neq 0$, there are topological quantum phases in the ground state, for which the winding number is an effective geometric order parameter [51]. The Hamiltonian in Eq. (1) can be further expressed in the Bogoliubov–de Gennes form of the momentum space [51,56]

$$H = \sum_{k=-M}^{M} (c_k^\dagger \quad c_{-k}) \mathcal{H}_k \begin{pmatrix} c_k \\ c_{-k}^\dagger \end{pmatrix}, \tag{9}$$

where $M = (L-1)/2$ for odd $L$, $\mathcal{H}_k = \vec{r}(k) \cdot \vec{\sigma}$ with $\vec{r}(k) = [0, y_k, z_k]$ and $\vec{\sigma} = (\sigma^x, \sigma^y, \sigma^z)$, and the vector $\vec{r}$ represents a two-dimensional magnetic field with the components $y_k = \gamma \sin\phi_k + \alpha\delta \sin(2\phi_k)$ and $z_k = \lambda - \cos\phi_k - \alpha \cos(2\phi_k)$. Zhang and Song established the connection between topological quantum phase and corresponding winding number [51]

$$\mathcal{N} = \frac{1}{2\pi} \oint (y\, dz - z\, dy)/|\vec{r}|^2, \tag{10}$$

which is an integer representing the direction and total times that the closed loop travels around the origin point in the $y$-$z$ plane [90]. The winding numbers can identify topological

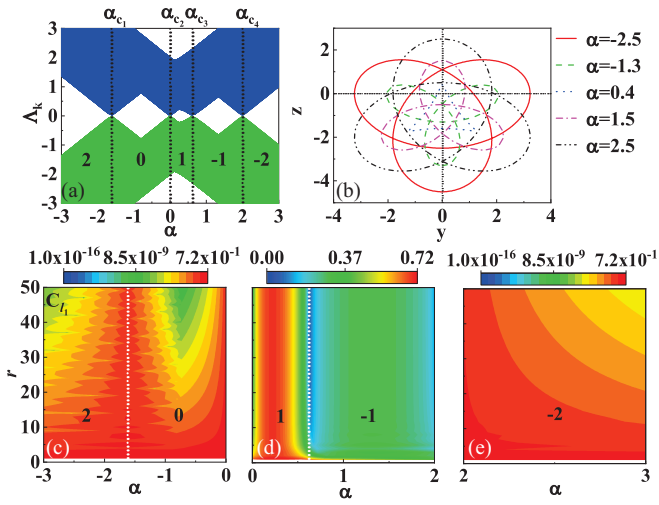


FIG. 4. Energy spectra, winding vector trajectories, and long-range quantum coherence $C_{l_1}(\alpha, r)$ in the extended Ising model with the parameters $\gamma = 1$, $\delta = -1$, and $\lambda = 1$ for the chain length $L = 1001$. (a) The energy spectra as a function of three-spin interaction $\alpha$ where the four critical points and five topological phases are labeled. (b) Different trajectories of the winding vectors in the $y$-$z$ plane correspond to the winding numbers 2, 0, 1, $-1$, and $-2$, respectively. (c)–(e) The behaviors of long-range two-site quantum coherence in different topological quantum phases.

quantum phases in the extended Ising model, and the critical points for the TQPTs are available by solving the characteristic equations [36].

Now, we study the connection between the long-range two-site quantum coherence and topological quantum phases in the extended Ising model. When the TQPTs are driven by the three-spin interaction $\alpha$, we choose the other system parameters to be $\gamma = 1$, $\delta = -1$, and $\lambda = 1$. As shown in Fig. 4(a), the energy spectra $\Lambda_k = \pm\sqrt{z_k^2 + y_k^2}$ are plotted for a finite chain length $L = 1001$, where the critical points $\alpha_{c_1} = (-\sqrt{5} - 1)/2, \alpha_{c_2} = 0, \alpha_{c_3} = (\sqrt{5} - 1)/2$, and $\alpha_{c_4} = 2$ are labeled. The trajectories of the typical winding vectors in the auxiliary $y$-$z$ plane are plotted in Fig. 4(b). As quantified by the $l_1$-norm measure, the two-site quantum coherence in the extended Ising system is

$$C_{l_1}(\rho_r) = 2(|y^+| + |y^-|), \tag{11}$$

where $y^{\pm} = (\langle\sigma_0^x\sigma_r^x\rangle \pm \langle\sigma_0^y\sigma_r^y\rangle)/4$ are the off-diagonal elements of two-site quantum state $\rho_r$ in Eq. (2). It is noted that the first-order derivative of adjacent two-site coherence $C_{l_1}$ can detect all the TQPTs in the extended Ising system (see Appendix F). Here we focus on the properties of the long-range two-site coherence in different topological phases. In Figs. 4(c)–4(e), we plot $C_{l_1}(\rho_r)$ as a function of three-spin interaction strength $\alpha$ and two-site distance $r$, where the different topological phases are labeled by the corresponding winding numbers. In the case of $\mathcal{N} = 2$, the coherence decays in the oscillating mode along with the increase of two-site distance for a given value of $\alpha$. But, in the case of $\mathcal{N} = -2$, the coherence decays in the gradual mode, although there exists initial oscillating for short two-site distance due to the influence of adjacent three-spin interactions. Moreover, the strength of $|\alpha|$ can change the decay rate in both topological phases of $\mathcal{N} = \pm 2$. In the case of $\mathcal{N} = 0$, the coherence can decay in both oscillating and gradual modes for different values of $\alpha$ as shown in Fig. 4(c). We further calculate the second-order derivative of the coherence $C_{l_1}(\alpha)$ for $r = 25$ in the topological phase $\mathcal{N} = 0$, where the diverging coherence derivative implies a symmetry-broken phase transition (see Appendix F). It is noted that the ground state of the XXT model we analyzed previously is also topologically trivial ($\mathcal{N} = 0$), where, as shown in Fig. 2, the quantum coherence exhibits two kinds of decay modes too.

The winding numbers in the extended Ising model characterize different topological orders and can identify corresponding topological phases. In the case of $\mathcal{N} = \pm 1$, we find that the two-site coherence exhibits a remarkable property, where the nonzero coherence will become stable for a given value of $\alpha$ after a slight decay of short two-site distances as shown in Fig. 4(d). In addition, the higher steady coherence exhibits in the phase $\mathcal{N} = 1$, and the lower steady coherence occurs in the phase $\mathcal{N} = -1$ (the relation between spin correlations and quantum coherence is further analyzed in Appendix G). The steady quantum coherence is the topologically protected long-range quantum resource, and we refer to it as quantum coherence freezing (QCF) phenomenon along with the two-site distance, which is different from the case of frozen quantum coherence under dynamical conditions [91–94].

Therefore, as shown in Fig. 4, the behaviors of long-range two-site coherence, such as damped oscillating and gradually decaying modes or the freezing mode, can serve as an effective diagnostic of topological quantum phases. In addition, we also investigate the TQPT driven by the external magnetic field $\lambda$, and find that the long-range coherence can diagnose the topological quantum phases too, where the coherence still exhibits the QCF phenomenon in the case $\mathcal{N} = 1$ (see the details in Appendix H).

In order to explain further topologically protected coherence exhibiting the QCF phenomenon, we consider a special case of the Hamiltonian with $\gamma = 1$ and $\lambda = \alpha = 0$, for which the winding number is $\mathcal{N} = 1$ and its ground state has an analytical form [51]

$$|G_1\rangle = \frac{1}{\sqrt{2}}\Big(\prod_{j\in e}|\nearrow\rangle_j \prod_{j\in o}|\swarrow\rangle_j + \prod_{j\in e}|\swarrow\rangle_j \prod_{j\in o}|\nearrow\rangle_j\Big), \tag{12}$$

where $\sigma_j^x|\nearrow\rangle_j(|\swarrow\rangle_j) = |\nearrow\rangle_j(-|\swarrow\rangle_j)$, and the summing targets $e$ and $o$ denote the even and odd number of sites, respectively. Its reduced quantum state of the $i$th and $j$th spins with distance $r$ is

$$\rho_r^{\mathcal{N}=1} = \frac{1}{4}\begin{pmatrix} 1 & 0 & 0 & -1 \\ 0 & 1 & -1 & 0 \\ 0 & -1 & 1 & 0 \\ -1 & 0 & 0 & 1 \end{pmatrix}, \tag{13}$$

which is a constant matrix independent of the two-site distance and has the steady coherence $C_{l_1}(\rho_r^{\mathcal{N}=1}) = 1$. Similarly, for the ground state $|G_{-1}\rangle$ [51] with the winding number $\mathcal{N} = -1$, we can derive the distance-independent two-site quantum coherence $C_{l_1}(\rho_r^{\mathcal{N}=-1}) = 1$.

## V. DISCUSSIONS

The above results for quantum coherence and quantum entanglement can be extended to other quantum resources, such as quantum discord, which can describe quantum correlations beyond entanglement [95–97]. The two-qubit quantum discord is quantified by the formula [19,20]

$$D_A(\rho_{AB}) = S(\rho_A) - S(\rho_{AB}) + \min_{\{E_k^A\}} \sum_k p_k S(\rho_{B|k}), \tag{14}$$

where the measurement $\{E_k^A\}$ is performed on subsystem $A$ with the minimum running over all the projection measurements, and $S(\cdot)$ is the von Neumann entropy. In the XXT model, we find that the discord $D_A(\rho_r)$ decays along with two-site distance in the gradual mode for the SL-I phase and in the oscillating mode for the SL-II phase (see Appendix I), indicating that quantum discord has the same functionality for the diagnostic of quantum phases. Furthermore, in the extended Ising model, although two-site entanglement is short range, quantum discord is long range which can identify topological quantum phases similar to the quantum coherence (see Appendix J). In particular, different from the dynamical case [98,99], we find a quantum discord freezing phenomenon in topological phases with the winding numbers $\mathcal{N} = \pm 1$.

The topologically protected quantum coherence and quantum discord, exhibiting the freezing property, are key resources in QIP. For example, quantum discord is related to the fidelity of quantum remote state preparation (RSP) [100] and the freezing quantum discord can keep the fidelity of RSP steady along with the distance of two sites, which makes long-range QIP possible. Moreover, assisted coherence distillation (ACD) [101,102] can convert bipartite quantum discord to single-party quantum coherence, and the freezing quantum discord can make a steady conversion to quantum coherence in the remote site, which can be further applied to quantum enhancement of metrology [103–105].

## VI. CONCLUSIONS AND OUTLOOK

In summary, we have demonstrated that the behaviors of long-range two-site quantum coherence, quantum entanglement, and quantum discord are able to diagnose quantum phases in many-body systems with symmetry-breaking and topological quantum phase transitions. In comparison with multipartite entanglement that needs to extract the scaling exponents of the QFI for global ground state [55,56], we provide a method for identifying quantum phases by the behaviors of long-range two-site quantum resources, which is feasible for the systems of cold atoms [66] and superconducting qubits [68] in the current or near-term experiments. The universality of our presented method is still an open problem and worth exploring in the future. Lastly, the topologically protected two-site quantum resources exhibit freezing phenomena, which have promising applications in long-range QIP.

## ACKNOWLEDGMENTS

This work was supported by NSF-China (Grants No. 11575051 and No. 11904078), Hebei NSF (Grants No. A2021205020 and No. A2019205266), Hebei 333 Talent Project (No. B20231005), the NSFC/RGC JRS grant (RGC Grant No. N-HKU774/21), the CRF (Grant No. C6009-20G), the GRF (Grants No. 17310622 and No. 17303023) of Hong Kong, and project of China Postdoctoral Science Foundation (Grant No. 2020M670683). W.L.M. acknowledges support from the Chinese Academy of Sciences (Grants No. E0SEBB11 and No. E27RBB11) and the National Natural Science Foundation of China (Grants No. 121743379 and No. E31Q02BG).

## APPENDIX A: DIAGONALIZATION PROCEDURE FOR THE HAMILTONIAN OF THE EXTENDED ISING MODEL

The Hamiltonian of the extended Ising model given in the main text has the form [51]

$$H = -\sum_{j=1}^{L}\Big[\frac{1+\gamma}{2}\sigma_j^x\sigma_{j+1}^x + \frac{1-\gamma}{2}\sigma_j^y\sigma_{j+1}^y + \lambda\sigma_j^z + \alpha\sigma_j^z\Big(\frac{1+\delta}{2}\sigma_{j-1}^x\sigma_{j+1}^x + \frac{1-\delta}{2}\sigma_{j-1}^y\sigma_{j+1}^y\Big)\Big], \tag{A1}$$

where $L$ is the total spin number in the spin chain, $\gamma$ is the anisotropic parameter of the nearest-neighbor couplings, $\lambda$ is the strength of external magnetic field, $\alpha$ and $\delta$ represent the strength and anisotropy of three-spin interactions, and $\sigma_j^x$, $\sigma_j^y$, and $\sigma_j^z$ are the Pauli operators on the $j$th spin. Next, we will give a brief review on the diagonalization procedure for this Hamiltonian [69–71].

The spin operators in the Hamiltonian can be mapped into the spinless fermion operators by introducing the Jordan-Wigner transformation [10]

$$\begin{aligned}\sigma_j^z &= 1 - 2c_j^\dagger c_j,\\ \sigma_j^x &= \prod_{l<j}(1-2c_l^\dagger c_l)(c_j^\dagger + c_j),\\ \sigma_j^y &= -i\prod_{l<j}(1-2c_l^\dagger c_l)(c_j^\dagger - c_j),\end{aligned} \tag{A2}$$

where $c_j^\dagger$ and $c_j$ are the spinless creation and annihilation operators. After substituting the expressions in Eq. (A2) into the Hamiltonian in Eq. (A1), we can obtain the form

$$\begin{aligned}H = &-\sum_{j=1}^{L}\lambda(1-2c_j^\dagger c_j)\\ &-\sum_{j=1}^{L}[\gamma(c_j^\dagger c_{j+1}^\dagger - c_j c_{j+1}) + c_j^\dagger c_{j+1} - c_j c_{j+1}^\dagger]\\ &-\sum_{j=1}^{L}\alpha(c_{j-1}^\dagger c_{j+1} - c_{j-1}c_{j+1}^\dagger)\\ &-\sum_{j=1}^{L}\alpha\delta(c_{j-1}^\dagger c_{j+1}^\dagger + c_{j-1}c_{j+1}).\end{aligned} \tag{A3}$$

Furthermore, the above Hamiltonian can be expressed in the momentum space by the Fourier transformation, and the Fourier transformation of fermion annihilation operator can

be written as

$$c_j = \frac{1}{\sqrt{L}} \sum_{k=-M}^{M} c_k \exp(-ij\phi_k), \tag{A4}$$

where $\phi_k = 2\pi k/L$ with $k = -M, \ldots, M$ and $M = (L-1)/2$ for odd $L$. After some derivation, we can rewrite the Hamiltonian in the form

$$\begin{aligned} H = & -\lambda L + 2(\lambda - 1 - \alpha)c_0^\dagger c_0 \\ & + \sum_{k=1}^{M} 2[\lambda - \cos\phi_k - \alpha\ \cos(2\phi_k)](c_k^\dagger c_k + c_{-k}^\dagger c_{-k}) \\ & + \sum_{k=1}^{M} 2i[\gamma\ \sin\phi_k + \alpha\delta\ \sin(2\phi_k)](c_k^\dagger c_{-k}^\dagger + c_k c_{-k}). \end{aligned} \tag{A5}$$

After further applying the Bogoliubov transformation, the Hamiltonian in Eq. (A5) can be transformed into the diagonal form

$$H = \sum_{k=-M}^{M} 2\Lambda_k \left(\eta_k^\dagger \eta_k - \frac{1}{2}\right), \tag{A6}$$

for which the energy spectra are $\pm\Lambda_k$ and

$$\Lambda_k = \sqrt{z(k)^2 + y(k)^2} \tag{A7}$$

with $z(k) = \lambda - \cos\phi_k - \alpha\ \cos(2\phi_k)$ and $y(k) = \gamma\ \sin\phi_k + \alpha\delta\ \sin(2\phi_k)$, and the mapping operator of Bogoliubov transformation is

$$\eta_k = \cos\frac{\theta_k}{2} c_{-k} - i\ \sin\frac{\theta_k}{2} c_k^\dagger, \tag{A8}$$

in which the coefficients are

$$\begin{aligned} \sin\frac{\theta_k}{2} &= \frac{\Lambda_k - z(k)}{\sqrt{2}\Lambda_k[\Lambda_k - z(k)]}, \\ \cos\frac{\theta_k}{2} &= \frac{y(k)}{\sqrt{2}\Lambda_k[\Lambda_k - z(k)]}, \end{aligned} \tag{A9}$$

with the parameter being

$$\theta_k = \arcsin\{-[\gamma\ \sin\phi_k + \alpha\delta\ \sin(2\phi_k)]/\Lambda_k\}. \tag{A10}$$

The above analysis completes the review of diagonalization procedure for the Hamiltonian of the extended Ising model.

## APPENDIX B: TWO-SITE REDUCED DENSITY MATRIX OF GROUND STATE IN THE EXTENDED ISING MODEL

In the extended Ising model, the two-site reduced density matrix of ground state for the $i$th and $j$th spins given in the main text has the form

$$\rho_r = \rho_{ij} = \begin{pmatrix} u^+ & 0 & 0 & y^- \\ 0 & z & y^+ & 0 \\ 0 & y^+ & z & 0 \\ y^- & 0 & 0 & u^- \end{pmatrix}, \tag{B1}$$

where $r = |j - i|$ denotes the distance between the two spins, and the nonzero matrix elements are $u^\pm = (1 \pm 2\langle\sigma^z\rangle + \langle\sigma_0^z\sigma_r^z\rangle)/4$, $z = (1 - \langle\sigma_0^z\sigma_r^z\rangle)/4$, and $y^\pm = (\langle\sigma_0^x\sigma_r^x\rangle \pm \langle\sigma_0^y\sigma_r^y\rangle)/4$, which can be calculated from the magnetization and spin correlation functions.

For the nonzero elements in $\rho_r$, the magnetization $\langle\sigma^z\rangle$ and two-site correlation functions $\langle\sigma_0^s\sigma_r^s\rangle$ with $s = x, y, z$ can be written as [69,70]

$$\begin{aligned} \langle\sigma^z\rangle &= G_0, \\ \langle\sigma_0^x\sigma_r^x\rangle &= \begin{vmatrix} G_{-1} & G_{-2} & \ldots & G_{-r} \\ G_0 & G_{-1} & \ldots & G_{-r+1} \\ \vdots & \vdots & \ddots & \vdots \\ G_{r-2} & G_{r-3} & \ldots & G_{-1} \end{vmatrix}, \\ \langle\sigma_0^y\sigma_r^y\rangle &= \begin{vmatrix} G_1 & G_0 & \ldots & G_{-r+2} \\ G_2 & G_1 & \ldots & G_{-r+3} \\ \vdots & \vdots & \ddots & \vdots \\ G_r & G_{r-1} & \ldots & G_1 \end{vmatrix}, \\ \langle\sigma_0^z\sigma_r^z\rangle &= \langle\sigma^z\rangle^2 - G_r G_{-r}, \end{aligned} \tag{B2}$$

where the $G_r$ function for the case of a finite chain length has the expression given in Eq. (3) of the main text and its formula for the case of the thermodynamic limit is presented in Eq. (4) of the main text. Therefore, according to Eqs. (B1) and (B2), the two-site quantum state $\rho_r$ can be obtained by calculating the $G_r$ functions and related determinants. Moreover, the two-spin correlations $\langle\sigma_0^x\sigma_r^x\rangle$ and $\langle\sigma_0^y\sigma_r^y\rangle$ in Eq. (B2) are the determinants of $G_r$ matrices, whose matrix dimension increases along with the two-spin distance $r$.

It should be noted that, in order to analyze the properties of quantum state and its quantum resource expediently, an analytical formula for the $G_r$ function is very desirable.

## APPENDIX C: GROUND-STATE PHASE DIAGRAM AND FERMI POINTS IN THE XXT MODEL

In the XXT model, by solving the energy equation $\Lambda_\phi = 0$ with $\phi \in \{0, \pi\}$ in the thermodynamic limit, we can obtain the two Fermi points $\phi_+$ and $\phi_-$ [as given in Eq. (5) of the main text] with the form

$$\phi_\pm(\alpha, \lambda) = \arccos\left[\frac{-1 \pm \sqrt{1 + 8\alpha^2 + 8\alpha\lambda}}{4\alpha}\right], \tag{C1}$$

where $\lambda$ is the external magnetic field and $\alpha$ is the strength of three-spin interactions. It should be noted that the Fermi points are required to be real numbers.

In Fig. 1 of the main text, we plot the ground-state phase diagram in the XXT model via the numbers of Fermi points. The ground-state phase diagram is composed of ferromagnetic phase, spin-liquid I (SL-I) phase, and spin-liquid II (SL-II) phase, where the phase boundaries are described by the critical lines $\lambda_{c_1} = \alpha + 1$, $\lambda_{c_2} = \alpha - 1$, and $\lambda_{c_3} = -(1 + 8\alpha^2)/8\alpha$ ($\alpha \geqslant 0.25$ for $\lambda_{c_3}$) as shown in the figure.

According to Eq. (C1), we calculate the Fermi point in the ferromagnetic phase and find that there is no real Fermi point. However, there are nonzero Fermi points in SL-I and SL-II phases, and we plot the Fermi points $\phi_\pm$ as the functions of external magnetic field $\lambda$ and the strength of three-spin interactions. As shown in Fig. 5, the Fermi point $\phi_+$ is nonzero in SL-I and SL-II phases, and the Fermi point $\phi_-$ is nonzero

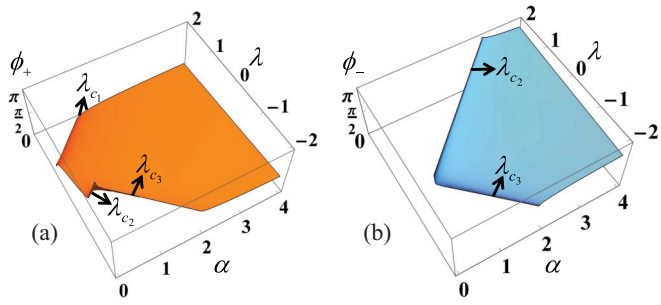


FIG. 5. The Fermi points (a) $\phi_+$ and (b) $\phi_-$ as the functions of external magnetic field $\lambda$ and the strength of three-spin interaction $\alpha$, where the boundaries $\lambda_1$, $\lambda_2$, and $\lambda_3$ are the critical lines representing the phase boundaries.

only in SL-II phase (with $\lambda_{c_1}$, $\lambda_{c_2}$, and $\lambda_{c_3}$ being the phase boundaries).

Combining the two regions of nonzero Fermi points in Figs. 5(a) and 5(b), we obtain that the number of Fermi points can not only detect the QPTs but also identify the three quantum phases, where there are two Fermi points in the SL-II phase, one in the SL-I phase and zero in ferromagnetic phase as illustrated in Fig. 1 of the main text.

## APPENDIX D: ANALYTICAL FORMULA FOR THE $G_r$ FUNCTION IN THE XXT MODEL

We consider the XXT model, for which the Hamiltonian shown in Eq. (1) of the main text has the parameters $\gamma = 0$, $\delta = 0$, and $\lambda \neq 0$. In the thermodynamic limit, the $G_r$ function has the form [71]

$$G_r = -\frac{1}{\pi}\int_0^{\pi} F(\lambda, \alpha, r)d\phi, \tag{D1}$$

where the integral kernel is

$$F(\lambda, \alpha, r) = \cos(\phi r)z/\Lambda_\phi \tag{D2}$$

in which the parameter is $\Lambda_\phi = \sqrt{z^2}$ with $z = \lambda - \cos\phi - \alpha\cos(2\phi)$.

The Fermi points [72,73] characterize the positions at which the energy $\Lambda_\phi$ is equal to zero, which plays a key role in the analysis on different quantum phases in the XXT model as shown in Fig. 1 of the main text. There are two Fermi points in the SL-II phase: one in the SL-I phase and zero in the ferromagnetic phase (the regions of Ferr-I and Ferr-II are the same phase). By solving the energy equation $\Lambda_\phi = 0$ with $\phi \in \{0, \pi\}$, we can obtain the two Fermi points $\phi_+$ and $\phi_-$ as given in Eq. (C1).

Next, according to the numbers and values of Fermi points, we will analyze the kernel functions $F(\lambda, \alpha, r)$ in different quantum phases. In the ferromagnetic phase, there is no Fermi point and we can demonstrate that $z(\phi) = \lambda - \cos\phi - \alpha\cos(2\phi)$ is positive in the region of Ferr-I and negative in the region of Ferr-II. Therefore, we have

$$F(\lambda, \alpha, r) = \frac{\cos(r\phi)[\lambda - \cos(\phi) - \alpha\cos(2\phi)]}{\sqrt{[\lambda - \cos(\phi) - \alpha\cos(2\phi)]^2}} = \begin{cases} \cos(r\phi), & \text{Ferr-I} \\ -\cos(r\phi), & \text{Ferr-II.} \end{cases} \tag{D3}$$

Substituting the result into the $G_r$ function in Eq. (C1), we can derive that $G_r = 0$ for the case of $r \neq 0$ and the nonzero $G_r$ corresponds to the case of $r = 0$. After some calculation, we obtain the analytical formula

$$G_r = \begin{cases} -\delta_{0r}, & \text{Ferr-I} \\ \delta_{0r}, & \text{Ferr-II.} \end{cases} \tag{D4}$$

In the SL-I phase, there is only one Fermi point $\phi_+$ which divides the function $z(\phi)$ into two parts. It can be demonstrated that $z(\phi)$ is negative in the region $\phi \in [0, \phi_+)$ and positive in the region $\phi \in [\phi_+, \pi]$. Therefore, according to Eq. (D1), we can have the kernel function

$$F(\lambda, \alpha, r) = \frac{\cos(r\phi)[\lambda - \cos(\phi) - \alpha\cos(2\phi)]}{\sqrt{[\lambda - \cos(\phi) - \alpha\cos(2\phi)]^2}} = \begin{cases} -\cos(r\phi), & \phi \in [0, \phi_+) \\ \cos(r\phi), & \phi \in [\phi_+, \pi]. \end{cases} \tag{D5}$$

By substituting the above expression into Eq. (C1), we can derive the analytical formula of $G_r$. In the case of $r \neq 0$, we have

$$G_r = \frac{1}{\pi}\int_0^{\phi_+}\cos(r\phi)d\phi - \frac{1}{\pi}\int_{\phi_+}^{\pi}\cos(r\phi)d\phi = \frac{2\sin(r\phi_+)}{\pi r}. \tag{D6}$$

When $r = 0$, the function is

$$G_r = \frac{1}{\pi}\int_0^{\phi_+} d\phi - \frac{1}{\pi}\int_{\phi_+}^{\pi} d\phi = \frac{2\phi_+}{\pi} - 1. \tag{D7}$$

Combining Eqs. (D6) and (D7), we can obtain the formula of $G_r$ in the SL-I phase

$$G_r = \frac{2\sin(r\phi_+)}{\pi r} - \delta_{0r}. \tag{D8}$$

In the SL-II phase, there are two Fermi points $\phi_+$ and $\phi_-$, which divide the function $z(\phi)$ into three parts where $z(\phi) > 0$ in the region $\phi \in [\phi_+, \phi_-]$ and $z(\phi) < 0$ in the regions $\phi \in [0, \phi_+) \cup (\phi_-, \pi]$. Then the kernel function in the SL-II phase has the form

$$F(\lambda, \alpha, r) = \frac{\cos(r\phi)[\lambda - \cos(\phi) - \alpha\cos(2\phi)]}{\sqrt{[\lambda - \cos(\phi) - \alpha\cos(2\phi)]^2}} = \begin{cases} -\cos(r\phi), & \phi \in [0, \phi_+) \\ \cos(r\phi), & \phi \in [\phi_+, \phi_-] \\ -\cos(r\phi), & \phi \in (\phi_-, \pi]. \end{cases} \tag{D9}$$

According to Eq. (C1), we can obtain the $G_r$ function in the case of $r \neq 0$:

$$G_r = \frac{1}{\pi}\int_0^{\phi_+}\cos(r\phi)d\phi - \frac{1}{\pi}\int_{\phi_+}^{\phi_-}\cos(r\phi)d\phi + \frac{1}{\pi}\int_{\phi_-}^{\pi}\cos(r\phi)d\phi = \frac{2[\sin(r\phi_+) - \sin(r\phi_-)]}{\pi r}, \tag{D10}$$

and the formula in the case of $r = 0$ is

$$G_r = \frac{1}{\pi}\int_0^{\phi_+} d\phi - \frac{1}{\pi}\int_{\phi_+}^{\phi_-} d\phi + \frac{1}{\pi}\int_{\phi_-}^{\pi} d\phi = \frac{2(\phi_+ - \phi_-)}{\pi} + 1. \tag{D11}$$

Combining Eqs. (D10) and (D11), we can obtain the analytical formula of $G_r$ function in the SL-II phase

$$G_r = \frac{2[\sin(r\phi_+) - \sin(r\phi_-)]}{\pi r} + \delta_{0r}. \tag{D12}$$

The expressions in Eqs. (D4), (D8), and (D12) constitute the analytical form of the $G_r$ function in the XXT model, which is given in Eq. (7) of the main text.

Based on the analytical formula of the $G_r$ function, we can expediently obtain the two-site reduced state $\rho_r$ and study further the properties of long-range two-site quantum resources in the reduced states, such as two-site quantum coherence, quantum entanglement, and quantum discord. For example, we have the two-site quantum coherence in the XXT model

$$C_{l_1}(\rho_r) = 2|y^+| = \left|\langle\sigma_0^x\sigma_r^x\rangle\right|, \tag{D13}$$

where the spin correlation $\langle\sigma_0^x\sigma_r^x\rangle$ is a determinant of $G_r$ matrix as shown in Eq. (B2). Since the determinant depends on the two-site distance, we are unable to obtain the closed-form expression of two-site quantum coherence in terms of two-site distance and model parameters. However, we can still obtain exactly the two-site quantum resources since for each fixed two-site distance we have a closed-form expression for the spin-spin correlation. In the case of $r = 3$ for the SL-I phase, we have $C_{l_1}(\rho_3) = |\langle\sigma_0^x\sigma_3^x\rangle|$, and the spin-spin correlation has the form

$$\begin{aligned}\left\langle\sigma_0^x\sigma_3^x\right\rangle &= \begin{vmatrix} G_{-1} & G_{-2} & G_{-3} \\ G_0 & G_{-1} & G_{-2} \\ G_1 & G_0 & G_{-1} \end{vmatrix} \\ &= G_{-1}^3 + G_{-2}^2 G_1 + G_0^2 G_{-3} - 2G_0 G_{-1} \\ &\quad \times G_{-2} - G_1 G_{-1} G_{-3},\end{aligned} \tag{D14}$$

where the $G_r$ function has the analytical form given in Eq. (D8). Substituting the expression of $G_r$ into the above equation, we are able to obtain the closed form of quantum coherence

$$\begin{aligned}C_{l_1}(\rho_3) &= \left|\langle\sigma_0^x\sigma_3^x\rangle\right| \\ &= \frac{2}{3\pi^3}\{|12(\pi - 2\phi_+)\cos(\phi_+)\sin^2(\phi_+) \\ &\quad - 2[\cos(2\phi_+) - 7]\sin^3(\phi_+) \\ &\quad + (\pi - 2\phi_+)^2\sin(3\phi_+)|\},\end{aligned} \tag{D15}$$

where $\phi_+$ is the Fermi point has the analytical expression in terms of system parameters as shown in Eq. (C1).

When we plot the two-site quantum coherence in Fig. 2 of the main text, the calculation method is similar and the value of coherence $C_{l_1}(\rho_r)$ for each fixed two-site distance can be determined exactly by the expression of spin-spin correlation in Eq. (B2) and our analytical formula of $G_r$ function in Eq. (7) of the main text.

## APPENDIX E: CONFIRMATION OF LONG-RANGE TWO-SITE ENTANGLEMENT IN THE XXT MODEL

In multipartite spin systems, two-site entanglement is often short range along with two-site distance and exhibits the phenomenon of entanglement sudden death [89]. Here, we study the entanglement property of the reduced state $\rho_r$ in the XXT model and analyze its long-range behavior of two-site entanglement. As quantified by the concurrence [11], we have

$$C(\rho_r) = \max\{0, 2(|y^+| - \sqrt{u^+u^-})\}, \tag{E1}$$

where $y^\pm$ and $u^\pm$ are the off-diagonal and diagonal elements of reduced state $\rho_r$ which can be calculated by the analytical formula of $G_r$. In the previous analysis, we have known that the coherence has the long-range property in this model, but whether there exists long-range two-site entanglement is still an open problem. We mainly consider the spin-liquid phases in the XXT model since the ground state in the ferromagnetic phase is the product state for which the concurrence of reduced state is zero.

According to Eq. (E1), we find that the concurrence is short range (no more than the next-nearest neighbor) in generic regions of SL-I and SL-II phases, but there still exists the long-range two-site entanglement for which the system parameters are close to the phase boundaries. Next, we give a detailed analysis on the confirmation of long-range two-site entanglement in the XXT model.

After some calculation, we can obtain the two-site concurrence in the SL-I phase

$$\begin{aligned}C(\rho_r) &= \max\left\{0, 2|y^+| - \frac{2}{\pi^2}\sqrt{(C_1 - E_1)(D_1 - E_1)}\right\} \\ &\approx \max\left\{0, C_{l_1}(\rho_r) - \frac{2}{\pi^2}\sqrt{C_1 D_1}\right\},\end{aligned} \tag{E2}$$

where the parameters are $C_1 = \phi_+^2$, $D_1 = (\pi - \phi_+)^2$, and $E_1 = \sin^2(r\phi_+)/r^2$ with $\phi_+$ being the Fermi point, and, in the second equation, we use the two-site coherence $C_{l_1}(\rho_r) = 2|y^+|$ in Eq. (6) of the main text and the approximation that the parameter $E_1$ tends to zero in the long-range case of two-site distance. Therefore, we know that the two-site concurrence is less than the corresponding two-site coherence. In Eq. (E2), the two-site concurrence can be expressed as the difference between the corresponding two-site coherence and the function of $C_1D_1$. When the term $C_1D_1$ is zero, the corresponding model parameters are in the critical lines representing phase boundaries (the red lines $\lambda_{c_1}$ and $\lambda_{c_2}$) as shown in the bottom of Fig. 6(a). Due to the two-site coherence being zero in the critical lines, the two-site concurrence will be zero when $C_1D_1 = 0$ according to the second expression in Eq. (E2).

When the term $C_1D_1$ is a small value and tends to zero, the corresponding model parameters are close to the phase boundaries $\lambda_{c_1}$ and $\lambda_{c_2}$ as shown in Fig. 6(a). In this case, the two-site quantum coherence is nonzero and decays gradually along with two-site distance. According to the expression of Eq. (E2), the competitive relation between the two-site coherence $C_{l_1}$ and the function of $C_1D_1$ determines the two-site entanglement (the minus sign between the two terms). It is noted that, for the given model parameters, both the coherence for $r = 1$ and the function of $C_1D_1$ are fixed values (we assume the value of $C_1D_1$ is small enough to be smaller than

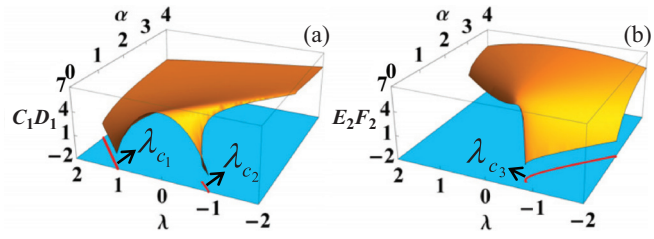


FIG. 6. (a) $C_1D_1$ and (b) $E_2F_2$ as the functions of the parameters $\alpha$ and $\lambda$, where the red lines on the bottom indicate the zero values for the two functions and correspond to the phase boundaries with the critical lines being $\lambda_{c_1}$, $\lambda_{c_2}(\alpha \leqslant 0.25)$, and $\lambda_{c_3}$, respectively.

that of the coherence for $r = 1$). Along with the increasing of two-site distance, the coherence decreases gradually but the term $C_1D_1$ keeps invariant, and the two-site entanglement becomes zero when the two competitive terms are equal. The smaller the value of $C_1D_1$, the larger the two-site distance of nonzero concurrence. Therefore, when the term $C_1D_1$ is close to the phase boundaries, there exists long-range two-site concurrence. In the main text, we choose the model parameters close to the critical lines and confirm the existence of long-range two-site entanglement up to the distance $r = 60$ as shown in Fig. 3(a) of the main text.

The case for two-site concurrence in the SL-II phase is similar, and we confirm the existence of long-range two-site entanglement for the system parameters close to the phase boundary between the SL-II phase and the Ferr-II phase. According to the formula in Eq. (E1), we can derive the two-site entanglement in the SL-II phase

$$C(\rho_r) = \max\left\{0, 2|y^+| - \frac{2}{\pi^2}\sqrt{(E_2 - G_2)(F_2 - G_2)}\right\}$$
$$\approx \max\left\{0, C_{l_1}(\rho_r) - \frac{2}{\pi^2}\sqrt{E_2F_2}\right\}, \tag{E3}$$

where the parameters are $E_2 = (\pi + \phi_+ - \phi_-)^2$, $F_2 = (\phi_+ - \phi_-)^2$ and $G_2 = [\sin(r\phi_+) - \sin(r\phi_-)]^2/r^2$ with $\phi_\pm$ being the two Fermi points, and we use the approximation that the parameter $G_2$ tends to zero in the long distance. After a similar analysis as that in the SL-I phase, we can obtain the result that the two-site entanglement is long-range in the case of $E_2F_2$ tending to zero (*i.e.*, the competitive relation between the two terms in the second expression of Eq. (E3) determines the long-range two-site entanglement). As shown in Fig. 6(b), $E_2F_2 = 0$ corresponds the critical line $\lambda_{c_3}$ (the red line in the bottom) which represents the phase boundary. In the main text, we choose a proper system parameters and confirm the long-range entanglement up to the two-site distance $r = 55$.

## APPENDIX F: DETECTION OF THE TQPTS BY THE $l_1$-NORM MEASURE OF QUANTUM COHERENCE

In the main text, we pointed out that the first-order derivative of adjacent two-site coherence $C_{l_1}(\rho_r)$ can detect the topological quantum phase transition in the extended Ising model. Here, we first consider the TQPTs driven by the three-spin interaction $\alpha$, and the other parameters in the model are chosen to be $\gamma = 1$, $\delta = -1$, and $\lambda = 1$, respectively. In

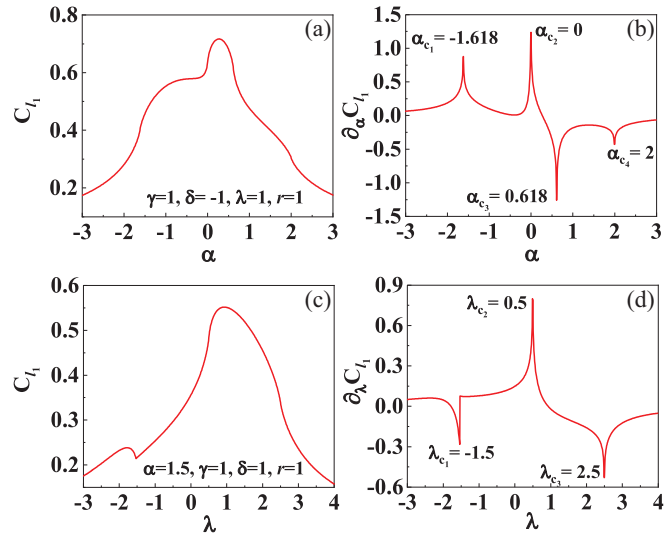


FIG. 7. The $l_1$ norm of quantum coherence $C_{l_1}$ and its derivative $\partial_\alpha C_{l_1}$ versus the three-spin interaction $\alpha$ [(a) and (b)] and external magnetic field $\lambda$ [(c) and (d)] for adjacent two-spin pair.

Figs. 7(a) and 7(b), we plot the $l_1$-norm coherence and its first-order derivative as a function of the parameter $\alpha$ for the adjacent spin pair. As shown in the figures, the quantum coherence $C_{l_1}(\rho_r)$ is a continuous function, but its first derivative exhibits the divergent behaviors where the divergent points just indicate the critical points $\alpha_{c_1} = (-\sqrt{5} - 1)/2$, $\alpha_{c_2} = 0$, $\alpha_{c_3} = (\sqrt{5} - 1)/2$, and $\alpha_{c_4} = 2$ for the TQPTs.

We also analyze the TQPTs driven by external magnetic field $\lambda$, and the other parameters in the model are chosen to be $\alpha = 1.5$, $\gamma = 1$, and $\delta = 1$, respectively. In Figs. 7(c) and 7(d), we plot the $l_1$-norm coherence and its first-order derivative as a function of the parameter $\lambda$ for the adjacent spin pair. As shown in the figures, the divergent points of the first-order derivative can indicate the critical points $\lambda_{c_1} = -1.5$, $\lambda_{c_2} = 0.5$, and $\lambda_{c_3} = 2.5$ for the TQPTs in the extended Ising model. Moreover, similar to the above cases, the TQPTs driven by the parameters $\gamma$ and $\delta$ can also be detected by the first-order derivative of $l_1$-norm quantum coherence for the adjacent two-spin pair.

In Fig. 4 of the main text, the two-site coherence in the topological quantum phase with the winding number $\mathcal{N} = 0$ exhibits two kinds of decay modes, which correspond to different symmetry-broken phases. As shown in Fig. 8, we plot the coherence and its second-order derivative as the functions of three-spin interaction $\alpha$ for the two-site distance $r = 25$, where the diverging coherence derivative in Fig. 8(b) implies a symmetry-broken quantum phase transition.

## APPENDIX G: RELATION BETWEEN SPIN CORRELATIONS AND QUANTUM COHERENCE IN TOPOLOGICAL QUANTUM PHASES

According to Eq. (11) of the main text, the long-range two-site quantum coherence $C_{l_1}(\rho_r)$ in the extended Ising model can be expressed as the function of spin correlations $\langle\sigma_0^x\sigma_r^x\rangle$ and $\langle\sigma_0^y\sigma_r^y\rangle$. It is pointed out in the main text that the behaviors of long-range quantum coherence (such as the damped

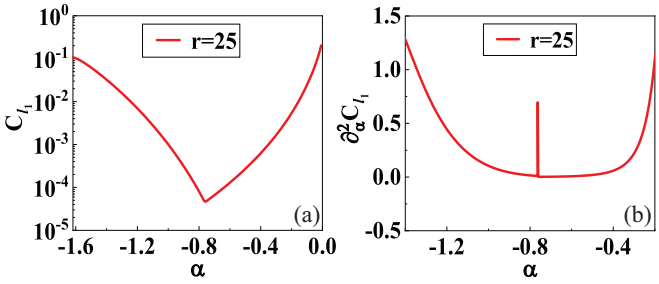


FIG. 8. In the topological phase $\mathcal{N}=0$, (a) the two-site coherence $C_{l_1}$ and (b) its second derivative $\partial^2 C_{l_1}$ versus the three-spin interaction $\alpha$ with the other model parameters $\gamma=1.0$, $\delta=-1.0$, and $\lambda=1.0$, respectively. The divergence of $\partial^2_\alpha C_{l_1}$ indicates a symmetry-broken quantum phase transition.

oscillating and gradually decaying modes as well as the freezing mode) can serve as the diagnostic tools for topological phases with different winding numbers. Here, we further study the relation between spin correlations and quantum coherence in the extended Ising model.

For the TQPTs driven by the three-spin interaction, we choose six typical values for the parameter $\alpha$, which correspond to the topological phases with the winding numbers $\mathcal{N}=0,\pm1,\pm2$, respectively. As shown in Fig. 9, two-site spin correlations $\langle\sigma_0^x\sigma_r^x\rangle$ (red dotted lines) and $\langle\sigma_0^y\sigma_r^y\rangle$ (blue triangle lines), the related moduli of spin-spin correlations, and the corresponding $l_1$-norm coherence $C_{l_1}(\rho_r)$s (black square lines) are plotted along with the increasing spin-spin distance in different phases. In comparison with the panels in the first row and the third row of this figure, we know that the behaviors of two-site quantum resources are not equivalent to those of the two-spin correlation functions (all the spin-spin correlations are oscillating in the first row), even if the two-site quantum coherence can be expressed as the simple functions of two-spin correlations. It should be noted that, in distinct quantum phases, one may expect the two-site spin correlation behaving differently, the more important issue is that how differently they behave and what kind of rules they obey. In our work, we reveal that the rules that two-site correlations obey are described by the two-site quantum coherence.

In the topological phase $\mathcal{N}=2$, the quantum coherence decays in the damped oscillating mode (see the first panel in the third row) and mainly comes from the modulus of spin correlation $|\langle\sigma_0^x\sigma_r^x\rangle|$, where the spin correlation $|\langle\sigma_0^y\sigma_r^y\rangle|$ will disappear after a short two-site distance (see the first panel in the second row). The coherence in the topological phase $\mathcal{N}=0$ can decay in both oscillating and gradual modes, where the damped oscillating coherence comes from spin correlation $|\langle\sigma_0^x\sigma_r^x\rangle|$, but the gradually decaying coherence is due to the spin correlation $|\langle\sigma_0^y\sigma_r^y\rangle|$ (see the panels and its insets in the second column of Fig. 9). In the topological phase $\mathcal{N}=-2$, the quantum coherence decays in the gradual mode and is mainly contributed by the modulus of spin correlation $|\langle\sigma_0^x\sigma_r^x\rangle|$, as shown in the bottom two panels in the fifth column of Fig. 9. Moreover, it was pointed out in the main text that the quantum coherence in topological phases $\mathcal{N}=\pm1$ will exhibit freezing phenomenon after a short-range distance. In the panels of the third and forth columns of Fig. 9, we plot the quantum coherence and its corresponding moduli of spin-spin correlations, where we find that the freezing coherence in the case of $\mathcal{N}=1$ is contributed by the modulus of two-spin correlation $|\langle\sigma_0^y\sigma_r^y\rangle|$ (blue triangle line) but the freezing resource in the case of $\mathcal{N}=-1$ comes from the modulus of two-spin correlation $|\langle\sigma_0^x\sigma_r^x\rangle|$ (red dotted line).

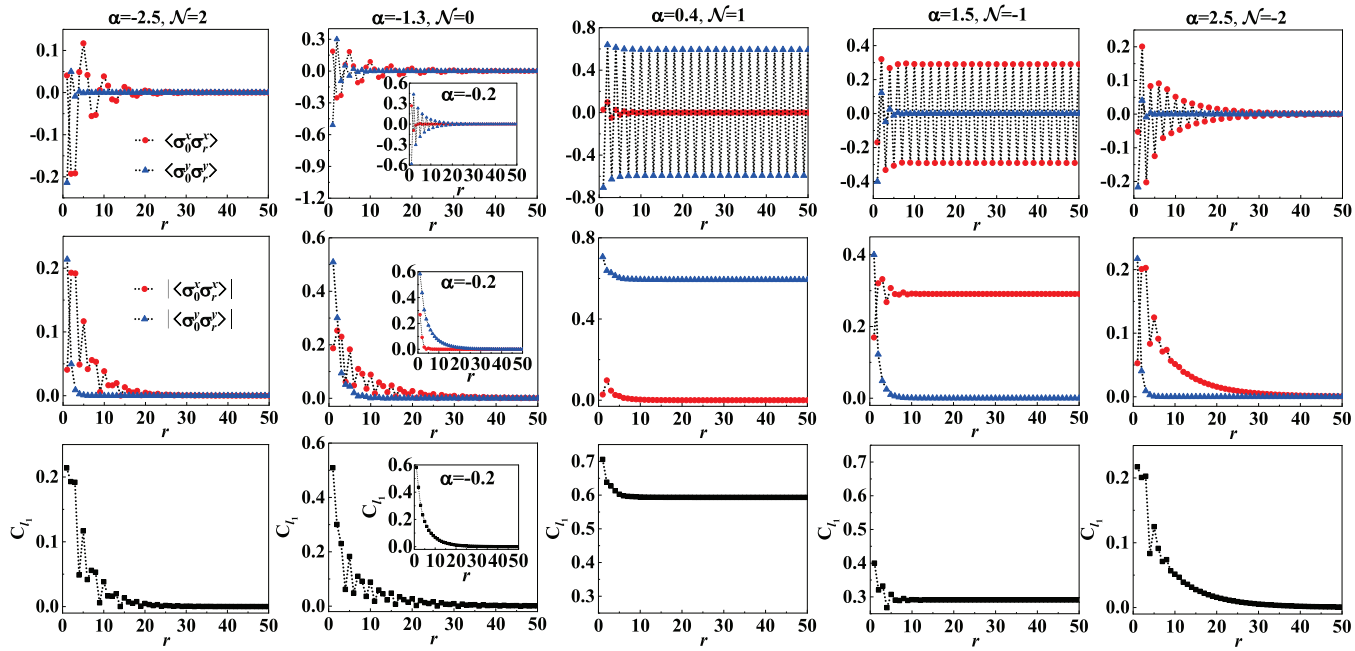


FIG. 9. Spin correlations (the first row), their absolute values (the second row), and quantum coherence (the third row) as the functions of two-site distance in the topological phases with winding numbers $\mathcal{N}=2,0,1,-1$, and $-2$, where the TQPTs are driven by three-spin interaction $\alpha$ with other system parameters being $\gamma=1$, $\delta=-1$, and $\lambda=1$, respectively. The long-range two-site quantum coherence is dominated by the modulus of spin-spin correlation $|\langle\sigma_0^x\sigma_r^x\rangle|$ or $|\langle\sigma_0^y\sigma_r^y\rangle|$ in different topological quantum phases.

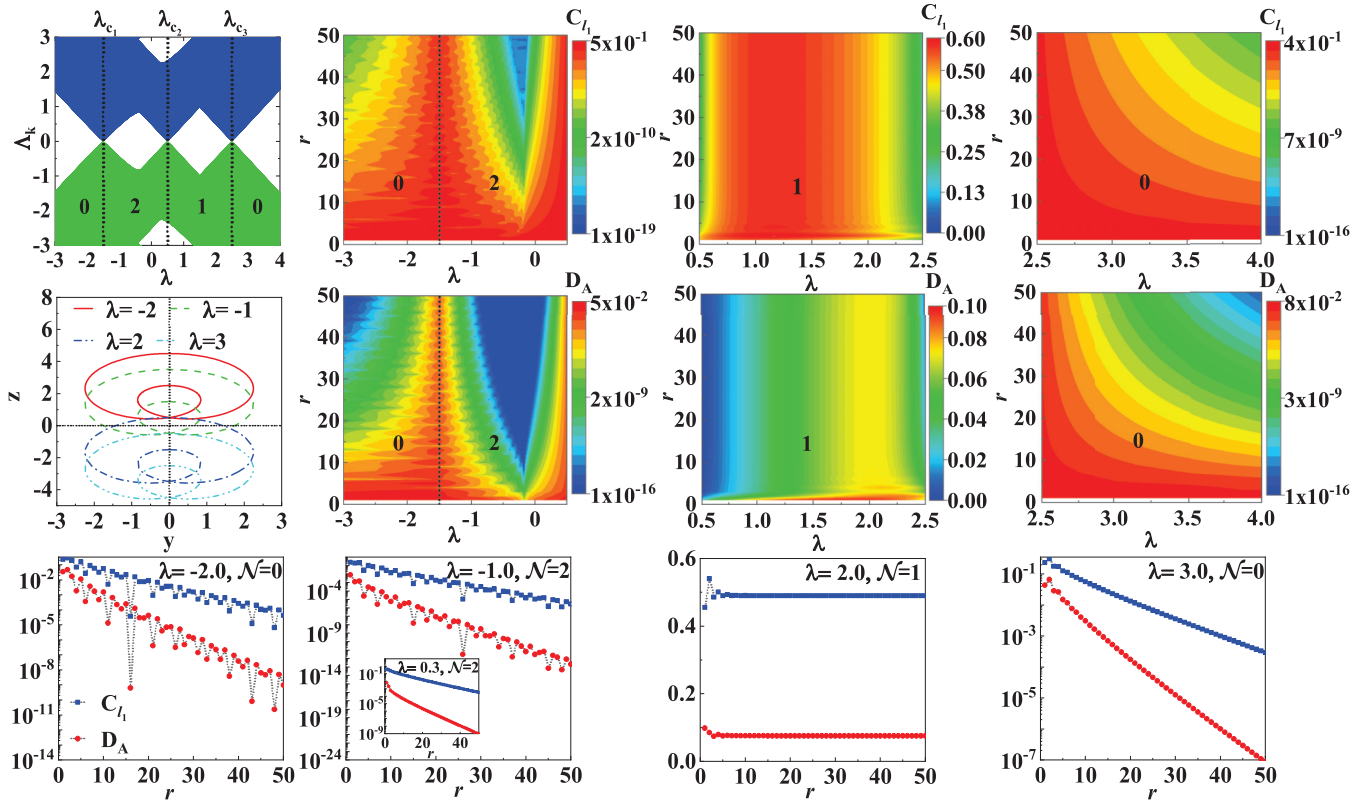


FIG. 10. Long-range properties of quantum coherence (the first row) and quantum discord (the second row) as a function of two-site distance and external magnetic field accompanied with the corresponding energy spectra $\Lambda_k(\lambda)$ and trajectories of winding vectors, and, in the third row, the oscillating-damped, gradual-damped, and freezing two-site quantum resources can serve as a set of effective diagnostic tools for topological phases in the extended Ising model.

## APPENDIX H: BEHAVIORS OF LONG-RANGE TWO-SITE QUANTUM RESOURCES IN THE TOPOLOGICAL PHASES DRIVEN BY EXTERNAL MAGNETIC FIELD

In this Appendix, we will study the long-range behaviors of quantum coherence and quantum discord in the topological phases driven by external magnetic field λ, where the other parameters in the extended Ising model are chosen to be $\alpha = 1.5, \gamma = 1, \delta = 1$. The critical points of the topological quantum phase transitions can be obtained via solving the characteristic equation [36]

$$3\xi^{-2}/2 + \xi^{-1} - \lambda = 0 \tag{H1}$$

for which the solutions are $\lambda_{c_1} = -1.5$ corresponding to $\xi_1 = \exp[\pm i \arccos(-1/3)]$, $\lambda_{c_2} = 0.5$ corresponding to $\xi_2 = -1$, and $\lambda_{c_3} = 2.5$ corresponding to $\xi_3 = 1$, respectively [106]. The two-site quantum coherence can be calculated according to the formula in Eq. (11) of the main text, and the corresponding quantum discord can be obtained by the method given in Eq. (J6) of Appendix J.

In Fig. 10, we plot the energy spectra of the system with a chain length $L = 1001$ (the three critical points and four regions of topological phases are labeled), the trajectories of the winding number vectors in the $x$-$y$ planes (corresponding to winding numbers $\mathcal{N} = 0$, 1, and 2), and the long-range properties of two-site quantum coherence and quantum discord. As shown in the first row of the figure, the $l_1$-norm coherence $C_{l_1}(\rho_r)$ in different regions of topological phases exhibits the damped oscillating, gradually decaying, and freezing modes along with two-site distance. In particular, the topologically protected quantum coherence in the phase $\mathcal{N} = 1$ will attain to a steady value after a short two-site distance. The case for two-site quantum discord $D_A(\rho_r)$ is similar, which exhibits the damped oscillating, gradually decaying, and freezing behaviors along with two-site distance in different regions of topological phases as shown in the second row of the figure. In the third row of the figure, we choose some typical values of external magnetic field λ and plot the long-range behaviors of quantum coherence and quantum discord, where the two kinds of quantum resources exhibit the similar decaying modes which further demonstrate that these long-range behaviors of quantum resources can serve as a set of effective diagnostic tools for topological quantum phases. Moreover, similar to the case in the topological quantum phases $\mathcal{N} = \pm 1$ driven by three-spin interaction $\alpha$, the topologically protected quantum resources in topological phase $\mathcal{N} = 1$ driven by magnetic field λ still exhibit the freezing phenomenon along with two-site distance.

## APPENDIX I: CHARACTERIZATION OF QUANTUM PHASES VIA THE LONG-RANGE TWO-SITE QUANTUM DISCORD IN THE XXT MODEL

Quantum discord is a kind of typical quantum correlation in quantum information processing and can be

written as [19,20]

$$D_A(\rho_{AB}) = S(\rho_A) - S(\rho_{AB}) + \min_{\{E_k^A\}} \sum_k p_k S(\rho_{B|k}), \quad \text{(I1)}$$

where the measurement $\{E_k^A\}$ is performed on subsystem $A$ with the minimum running over all the projection measurements, $S(\sigma) = -\mathrm{Tr}\sigma \log\sigma$ is the von Neumann entropy and $\rho_{B|k} = \mathrm{Tr}_A[E_k^A \rho_{AB} E_k^A / \mathrm{Tr}(E_k^A \rho_{AB} E_k^A)]$ is the output state of subsystem $B$ after the measurement $E_k^A$ with the probability being $p_k = \mathrm{Tr}(E_k^A \rho_{AB} E_k^A)$.

In the XXT model, the two-qubit reduced state $\rho_{AB} = \rho_r$ has the form given in Eq. (2) of the main text, for which the single-qubit reduced state for subsystem $A$ is

$$\rho_A = \begin{pmatrix} u^+ + z & 0 \\ 0 & u^- + z \end{pmatrix}. \quad \text{(I2)}$$

After some derivation, we can obtain the von Neumann entropies for the reduced states $\rho_A$ and $\rho_{AB}$,

$$\begin{aligned} S(\rho_A) &= -\mathrm{Tr}\rho_A \log_2 \rho_A \\ &= -\frac{1}{2}(1 + \langle\sigma^z\rangle) \log_2 \left[\frac{1}{2}(1 + \langle\sigma^z\rangle)\right] \\ &\quad -\frac{1}{2}(1 - \langle\sigma^z\rangle) \log_2 \left[\frac{1}{2}(1 - \langle\sigma^z\rangle)\right], \end{aligned} \quad \text{(I3)}$$

and

$$\begin{aligned} S(\rho_{AB}) &= -\mathrm{Tr}\rho_r \log_2 \rho_r \\ &= -z_1 \log_2 z_1 - z_2 \log_2 z_2 \\ &\quad -u^+ \log_2 u^+ - u^- \log_2 u^-, \end{aligned} \quad \text{(I4)}$$

where $z_1 = z + y^+ = (1 + 2\langle\sigma_0^x \sigma_r^x\rangle - \langle\sigma_0^z \sigma_r^z\rangle)/4$, $z_2 = z - y^+ = (1 - 2\langle\sigma_0^x \sigma_r^x\rangle - \langle\sigma_0^z \sigma_r^z\rangle)/4$, and $u^\pm = (1 \pm 2\langle\sigma^z\rangle + \langle\sigma_0^z \sigma_r^z\rangle)/4$.

The third term in Eq. (I1) is the measurement-induced conditional entropy, where the optimal measurement on subsystem $A$ can be determined via the method presented by Chen *et al.* [107]. The two-qubit reduced state $\rho_{AB} = \rho_r$ in the XXT model has the X shape for which the optimal measurement for $D_A(\rho_{AB})$ is $\sigma_z$ if

$$(y^+)^2 \leqslant (u^+ - z)(u^- - z), \quad \text{(I5)}$$

and the optical measurement is $\sigma_x$ if

$$|\sqrt{u^+ u^-} - \sqrt{z^2}| \leqslant |y^+|, \quad \text{(I6)}$$

where the parameters $y^\pm$, $u^\pm$, and $z$ are the matrix elements of $\rho_r$ given in Eq. (2) of the main text. Therefore, the measurement-induced conditional entropy in Eq. (I1) is

$$\widetilde{S}(B|A) = \min_{\{\sigma_x^k \text{ or } \sigma_z^k\}} \sum_k p_k S(\rho_{B|k}), \quad \text{(I7)}$$

where $\sigma_x^k$ and $\sigma_z^k$ with $k = 0$ and 1 are corresponding measurement operators for the Pauli measurements, and the related conditional entropies are

$$\sum_{\{\sigma_x^k\}} p_k S(\rho_{B|k}) = -\lambda_+ \log_2(\lambda_+) - \lambda_- \log_2(\lambda_-), \quad \text{(I8)}$$

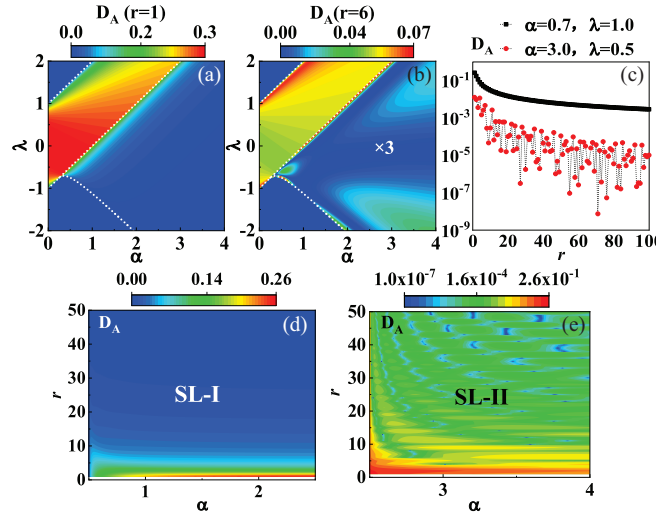


FIG. 11. The two-site quantum discord in the XXT model. $D_A(\alpha, \lambda)$ for two-site distances: (a) $r = 1$ and (b) $r = 6$ with the white dashed lines being the phase boundaries. In (c), two set parameters are chosen for $D_A(r)$ in the SL-I and SL-II phases, and the gradually decaying and damped oscillating modes of the quantum discord along with two-site distance are further illustrated in (d) and (e).

in which the parameters are $\lambda_\pm = (1 \pm \sqrt{\langle\sigma_0^x \sigma_r^x\rangle^2 + \langle\sigma^z\rangle^2})/2$, and

$$\sum_{\{\sigma_z^k\}} p_k S(\rho_{B|k}) = -\sum_{i=+,-} p_i(\xi_i \log_2 \xi_i + \eta_i \log_2 \eta_i), \quad \text{(I9)}$$

in which the probabilities and the corresponding eigenvalues of subsystem $B$ are

$$\begin{aligned} p_\pm &= (1 \pm \langle\sigma^z\rangle)/2, \\ \xi_\pm &= \left(1 - \left\langle\sigma_0^z \sigma_r^z\right\rangle\right)/[2(1 \pm \langle\sigma^z\rangle)], \\ \eta_\pm &= \left(1 \pm 2\langle\sigma^z\rangle + \left\langle\sigma_0^z \sigma_r^z\right\rangle\right)/[2(1 \pm \langle\sigma^z\rangle)]. \end{aligned} \quad \text{(I10)}$$

Combining Eqs. (I7), (I3) and (I4), we can calculate the two-site quantum discord for the reduced state $\rho_r$ in the XXT model.

Next, we study the long-range property of quantum discord in the XXT model. As shown in Figs. 11(a) and 11(b), we plot quantum coherence $D_A(\rho_r)$ as a function of magnetic field $\lambda$ and interaction strength $\alpha$ for spin-spin distances $r = 1$ and 6. We can distinguish the SL-I and SL-II phases from the ferromagnetic phase having zero coherence, and the change patterns of $D_A$ are different where $D_A$ is gradual in SL-I phase and oscillating in SL-II phase. The intrinsic reason is that the quantum discord decays along with the two-site distance $r$ in the gradual mode for SL-I phase but in the oscillating mode for SL-II phase as shown in Fig. 11(c). Therefore, the gradually decaying and damped oscillating mode of quantum discord can serve as an effective diagnostic of quantum phases as illustrated by Figs. 11(d) and 11(e).

## APPENDIX J: BEHAVIORS OF LONG-RANGE QUANTUM DISCORD IN THE TOPOLOGICAL PHASES DRIVEN BY THREE-SPIN INTERACTIONS

In the main text, we have analyzed the properties of different topological phases with the behaviors of long-range two-site quantum coherence. Here, we will further demonstrate that the behaviors of long-range quantum discord have the same functionality for characterization on the topological phases driven by three-spin interactions. The expression of two-site reduced state ($\rho_r = \rho_{AB}$) is given in Eq. (2) of the main text, and the related quantum discord $D_A$ can be calculated according to the formula in Eq. (14) of the main text where the von Neumann entropies $S(\rho_A)$ and $S(\rho_{AB})$ can be obtained via some direct calculation, but the measurement-induced conditional entropy

$$\widetilde{S}(B|A) = \min_{\{E_k^A\}} \sum_k p_k S(\rho_{B|k}) \tag{J1}$$

needs to be optimized by all the projective measurements $\{E_k^A\}$ on the subsystem $A$.

Although the two-site reduced state $\rho_r$ is still X shape in the extended Ising model ($\gamma \neq 0$ and $\delta \neq 0$), the method presented in Ref. [107] for selecting the optimal measurement of $D_A(\rho_{AB})$ is not applicable due to the condition on matrix elements $|y^+ + y^-| \geqslant |y^+ - y^-|$ not being satisfied. Therefore, in order to calculate the measurement-induced conditional entropy in quantum discord, we will consider the situation for all the projective measurements in which the measurement operator can be written as [32,108]

$$E_i^A = V|i\rangle\langle i|V^\dagger, \tag{J2}$$

where $\{|i\rangle\}$ is the standard computational basis $\{|0\rangle, |1\rangle\}$ and the unitary transformation matrix $V$ has the form

$$V = \begin{pmatrix} \cos\frac{\theta}{2} & e^{-i\phi}\sin\frac{\theta}{2} \\ e^{i\phi}\sin\frac{\theta}{2} & -\cos\frac{\theta}{2} \end{pmatrix}, \tag{J3}$$

in which the parameters satisfy $0 \leqslant \theta \leqslant \pi$ and $0 \leqslant \phi < 2\pi$. In this case, the quantum discord $D_A$ can be obtained via the optimization of parameters $\theta$ and $\phi$ in measurement-induced conditional entropy. After carefully numerical verifications similar to those of Ref. [32], we find that the optimal projective measurements in Eq. (J1) correspond to the following three cases:

$$\begin{aligned} &E_{k(\mathrm{I})}^A: \ \theta = \pi/2, \ \phi = \pi/2, \\ &E_{k(\mathrm{II})}^A: \ \theta = \pi/2, \ \phi = 0, \\ &E_{k(\mathrm{III})}^A: \ \theta = 0, \ \phi = 0, \end{aligned} \tag{J4}$$

with $k = 1, 2$, and then the measurement-induced conditional entropy is

$$\widetilde{S}(B|A) = \min_{\{E_{k(\mathrm{I})}^A, E_{k(\mathrm{II})}^A, E_{k(\mathrm{III})}^A\}} \sum_k p_k S(\rho_{B|k}). \tag{J5}$$

In Fig. 12, we choose three typical quantum states of $\rho_r$ for which the optimal measurements for $\widetilde{S}(B|A)$ correspond to $E_{k(\mathrm{I})}^A$, $E_{k(\mathrm{II})}^A$, and $E_{k(\mathrm{III})}^A$, respectively.

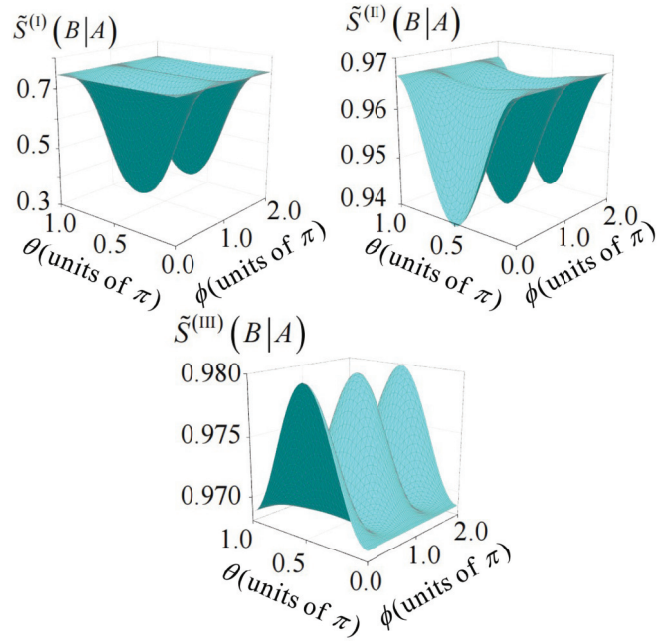


FIG. 12. The measurement-induced conditional entropies $\widetilde{S}(B|A)$ for three typical quantum states $\rho_r$ ($r = 2$) which correspond to optimal projective measurements: (a) $\{E_{k(\mathrm{I})}^A\}$ for $\rho_r$ with parameters $\gamma = 1$, $\delta = -1$, $\lambda = 1$, and $\alpha = 0.1$, (b) $\{E_{k(\mathrm{II})}^A\}$ for $\rho_r$ with parameters $\gamma = 1$, $\delta = -1$, $\lambda = 1$, and $\alpha = -2.5$, and (c) $\{E_{k(\mathrm{III})}^A\}$ for $\rho_r$ with parameters $\gamma = 1$, $\delta = -2$, $\lambda = -0.3$, and $\alpha = 1$.

Based on the previous analysis, we can derive the two-site quantum discord

$$D_A(\rho_r) = \widetilde{S}(B|A) - S(B|A), \tag{J6}$$

where the quantum condition entropy $S(B|A) = S(AB) - S(A)$ and the measurement-induced conditional entropy $\widetilde{S}(B|A)$ is given by Eq. (J5) in which

$$\begin{aligned} \widetilde{S}^{(\mathrm{I})}(B|A) &= \sum_{E_{k(\mathrm{I})}^A} p_k S(\rho_{B|k}) \\ &= -\beta_+ \log_2(\beta_+) - \beta_- \log_2(\beta_-) \end{aligned} \tag{J7}$$

with $\beta_\pm = [1 \pm (\langle\sigma_0^y\sigma_r^y\rangle^2 + \langle\sigma^z\rangle^2)^{1/2}]/2$,

$$\begin{aligned} \widetilde{S}^{(\mathrm{II})}(B|A) &= \sum_{E_{k(\mathrm{II})}^A} p_k S(\rho_{B|k}) \\ &= -\lambda_+ \log_2(\lambda_+) - \lambda_- \log_2(\lambda_-) \end{aligned} \tag{J8}$$

with $\lambda_\pm = [1 \pm (\langle\sigma_0^x\sigma_r^x\rangle^2 + \langle\sigma^z\rangle^2)^{1/2}]/2$, and

$$\begin{aligned} \widetilde{S}^{(\mathrm{III})}(B|A) &= \sum_{E_{k(\mathrm{III})}^A} p_k S(\rho_{B|k}) \\ &= -\sum_{i=+,-} p_i(\xi_i \log_2 \xi_i + \eta_i \log_2 \eta_i) \end{aligned} \tag{J9}$$

with $p_\pm = (1 \pm \langle\sigma^z\rangle)/2$, $\xi_\pm = (1 - \langle\sigma_0^z\sigma_r^z\rangle)/[2(1 \pm \langle\sigma^z\rangle)]$, and $\eta_\pm = (1 \pm 2\langle\sigma^z\rangle + \langle\sigma_0^z\sigma_r^z\rangle)/[2(1 \pm \langle\sigma^z\rangle)]$.

In Figs. 13(a)–13(c), we plot quantum discord $D_A(\rho_r)$ as a function of three-spin interaction $\alpha$ and two-site distance $r$, where the different topological phases are labeled by the corresponding winding numbers. In the case of $\mathcal{N} = 2$,

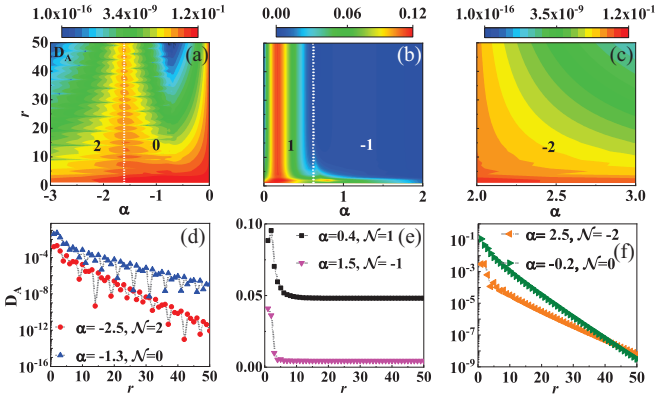


FIG. 13. (a)–(c) The quantum discord $D_A(\rho_r)$ as a function of three-spin interaction $\alpha$ and two-site distance $r$ in different topological phases with winding numbers $\mathcal{N} = 0, \pm 1$, and $\pm 2$ where the other parameters are chosen to be $\gamma = 1$, $\delta = -1$, and $\lambda = 1$. (d)–(f) The behaviors of long-range two-site discord for some typical values of $\alpha$ in the five quantum phases.

the quantum discord decays in the oscillating mode along with two-site distance for a given value of $\alpha$. However, in the case of $\mathcal{N} = -2$, quantum discord decays in the gradual mode after a short two-site distance as shown in Fig. 13(c). Moreover, the quantum discord in topological phase $\mathcal{N} = 0$ can decay in both oscillating and gradual modes as shown in Fig. 13(a). In particular, given a value of $\alpha$, the nonzero quantum discord in topological phases $\mathcal{N} = \pm 1$ exhibits quantum correlation freezing phenomenon after a short two-site distance as shown in Fig. 13(b). In the generic case, the freezing quantum discord in topological phase $\mathcal{N} = 1$ has a larger value than that of quantum discord in topological phase $\mathcal{N} = -1$. In Figs. 13(d)–13(f), we select some typical values in different topological phases and plot the long-range behaviors of quantum discord, where the damped oscillating, gradually decaying, and freezing modes of $D_A(\rho_r)$ can serve as the effective diagnostic tools for quantum phases. It should be noted that the steady quantum discord is the topologically protected long-range quantum correlation and has the potential applications in quantum computation and quantum communication.


[1] E. Chitambar and G. Gour, Quantum resource theories, Rev. Mod. Phys. **91**, 025001 (2019).

[2] R. Horodecki, P. Horodecki, M. Horodecki, and K. Horodecki, Quantum entanglement, Rev. Mod. Phys. **81**, 865 (2009).

[3] K. Modi, A. Brodutch, H. Cable, T. Paterek, and V. Vedral, The classical-quantum boundary for correlations: Discord and related measures, Rev. Mod. Phys. **84**, 1655 (2012).

[4] A. Streltsov, G. Adesso, and M. B. Plenio, Colloquium: Quantum coherence as a resource, Rev. Mod. Phys. **89**, 041003 (2017).

[5] M.-L. Hu, X. Hu, J. Wang, Y. Peng, Y.-R. Zhang, and H. Fan, Quantum coherence and geometric quantum discord, Phys. Rep. **762**, 1 (2018).

[6] L. Amico, R. Fazio, A. Osterloh, and V. Vedral, Entanglement in many-body systems, Rev. Mod. Phys. **80**, 517 (2008).

[7] J. Eisert, M. Cramer, and M. B. Plenio, Colloquium: Area laws for the entanglement entropy, Rev. Mod. Phys. **82**, 277 (2010).

[8] G. De Chiara and A. Sanpera, Genuine quantum correlations in quantum many-body systems: A review of recent progress, Rep. Prog. Phys. **81**, 074002 (2018).

[9] D. A. Abanin, E. Altman, I. Bloch, and M. Serbyn, Colloquium: Many-body localization, thermalization and entanglement, Rev. Mod. Phys. **91**, 021001 (2019).

[10] S. Sachdev, *Quantum Phase Transitions* (Cambridge University Press, Cambridge, UK, 2011).

[11] W. K. Wootters, Entanglement of formation of an arbitrary state of two qubits, Phys. Rev. Lett. **80**, 2245 (1998).

[12] A. Osterloh, L. Amico, G. Falci, and R. Fazio, Scaling of entanglement close to a quantum phase transition, Nature (London) **416**, 608 (2002).

[13] T. Baumgratz, M. Cramer, and M. B. Plenio, Quantifying coherence, Phys. Rev. Lett. **113**, 140401 (2014).

[14] J. Åberg, Quantifying superposition, arXiv:quant-ph/0612146.

[15] Y. Yao, X. Xiao, L. Ge, and C. P. Sun, Quantum coherence in multipartite systems, Phys. Rev. A **92**, 022112 (2015).

[16] C. Napoli, T. R. Bromley, M. Cianciaruso, M. Piani, N. Johnston, and G. Adesso, Robustness of coherence: An operational and observable measure of quantum Coherence, Phys. Rev. Lett. **116**, 150502 (2016).

[17] J.-J. Chen, J. Cui, Y.-R. Zhang, and H. Fan, Coherence susceptibility as a probe of quantum phase transitions, Phys. Rev. A **94**, 022112 (2016).

[18] K. Bu, U. Singh, S.-M. Fei, A. K. Pati, and J. Wu, Maximum relative entropy of coherence: An operational coherence measure, Phys. Rev. Lett. **119**, 150405 (2017).

[19] H. Ollivier and W. H. Zurek, Quantum discord: A measure of the quantumness of correlations, Phys. Rev. Lett. **88**, 017901 (2001).

[20] L. Henderson and V. Vedral, Classical, quantum and total correlations, J. Phys. A: Math. Gen. **34**, 6899 (2001).

[21] V. Coffman, J. Kundu, and W. K. Wootters, Distributed entanglement, Phys. Rev. A **61**, 052306 (2000).

[22] D. A. Meyer and N. R. Wallach, Global entanglement in multiparticle systems, J. Math. Phys. **43**, 4273 (2002).

[23] T.-C. Wei and P. M. Goldbart, Geometric measure of entanglement and applications to bipartite and multipartite quantum states, Phys. Rev. A **68**, 042307 (2003).

[24] Y.-C. Ou and H. Fan, Monogamy inequality in terms of negativity for three-qubit states, Phys. Rev. A **75**, 062308 (2007).

[25] Y.-K. Bai, M.-Y. Ye, and Z. D. Wang, Entanglement monogamy and entanglement evolution in multipartite systems, Phys. Rev. A **80**, 044301 (2009).

[26] Y.-K. Bai, Y.-F. Xu, and Z. D. Wang, General monogamy relation for the entanglement of formation in multiqubit systems, Phys. Rev. Lett. **113**, 100503 (2014).

[27] C. Eltschka and J. Siewert, Quantifying entanglement resources, J. Phys. A: Math. Theor. **47**, 424005 (2014).

[28] L.-H. Ren, M. Gao, J. Ren, Z. D. Wang, and Y.-K. Bai, Resource conversion between operational coherence and multipartite entanglement in many-body systems, New J. Phys. **23**, 043053 (2021).

[29] T.-C. Wei, D. Das, S. Mukhopadyay, S. Vishveshwara, and P. M. Goldbart, Global entanglement and quantum criticality in spin chains, Phys. Rev. A **71**, 060305(R) (2005).

[30] T. R. de Oliveira, G. Rigolin, and M. C. de Oliveira, Genuine multipartite entanglement in quantum phase transitions, Phys. Rev. A **73**, 010305(R) (2006).

[31] T. R. de Oliveira, G. Rigolin, M. C. de Oliveira, and E. Miranda, Multipartite entanglement signature of quantum phase transitions, Phys. Rev. Lett. **97**, 170401 (2006).

[32] Y.-C. Li and H.-Q. Lin, Thermal quantum and classical correlations and entanglement in the *XY* spin model with three-spin interaction, Phys. Rev. A **83**, 052323 (2011).

[33] S. Campbell, J. Richens, N. L. Gullo, and T. Busch, Criticality, factorization, and long-range correlations in the anisotropic *XY* model, Phys. Rev. A **88**, 062305 (2013).

[34] M. Hofmann, A. Osterloh, and O. Gühne, Scaling of genuine multiparticle entanglement close to a quantum phase transition, Phys. Rev. B **89**, 134101 (2014).

[35] S. M. Giampaolo and B. C. Hiesmayr, Genuine multipartite entanglement in the cluster-Ising model, New J. Phys. **16**, 093033 (2014)

[36] S.-P. Li and Z.-H. Sun, Local and intrinsic quantum coherence in critical systems, Phys. Rev. A **98**, 022317 (2018).

[37] K. C. Tan, Idendifying quantum phase transitions via geometric measures of nonclassicality, Phys. Rev. A **102**, 022421 (2020).

[38] M.-L. Hu, Y.-Y. Gao, and H. Fan, Steered quantum coherence as a signature of quantum phase transitions in spin chains, Phys. Rev. A **101**, 032305 (2020).

[39] R. R. Soldati, M. T. Mitchison, and G. T. Landi, Multipartite quantum correlations in a two-mode Dicke model, Phys. Rev. A **104**, 052423 (2021).

[40] L.-L. Su, J. Ren, Z. D. Wang, and Y.-K. Bai, Long-range multipartite quantum correlations and factorization in a one-dimensional spin-1/2 *XY* chain, Phys. Rev. A **106**, 042427 (2022).

[41] Y.-C. Li, Y.-H. Zhou, Y. Zhang, Y.-K. Bai, and H.-Q. Lin, Multipartite entanglement serves as a faithful detector for quantum phase transitions, New J. Phys. **26**, 023031 (2024).

[42] B. Zeng, X. Chen, D.-L. Zhou, and X.-G. Wen, *Quantum Information Meets Quantum Matter: From Quantum Entanglement to Topological Phases of Many-Body Systems* (Springer, New York, 2019).

[43] N. Read and D. Green, Paired states of fermions in two dimensions with breaking of parity and time-reversal symmetries and the fractional quantum Hall effect, Phys. Rev. B **61**, 10267 (2000).

[44] G. E. Volovik, *The Universe in a Helium Droplet* (Oxford University Press, New York, 2003).

[45] A. Kitaev, Anyons in an exactly solved model and beyond, Ann. Phys. **321**, 2 (2006).

[46] X.-G. Wen, *Quantum Field Theory of Many-Body Systems* (Oxford University Press, New York, 2004).

[47] X.-Y. Feng, G.-M. Zhang, and T. Xiang, Topological characterization of quantum phase transitions in a spin-1/2 model, Phys. Rev. Lett. **98**, 087204 (2007).

[48] S. Trebst, P. Werner, M. Troyer, K. Shtengel, and C. Nayak, Breakdown of a topological phase: Quantum phase transition in a loop gas model with tension, Phys. Rev. Lett. **98**, 070602 (2007).

[49] D. H. Lee, G.-M. Zhang, and T. Xiang, Edge solitons of topological insulators and fractionalized quasiparticles in two dimensions, Phys. Rev. Lett. **99**, 196805 (2007).

[50] H. Li and F. D. M. Haldane, Entanglement spectrum as a generalization of entanglement entropy: Identification of topological order in non-abelian fractional quantum hall effect states, Phys. Rev. Lett. **101**, 010504 (2008).

[51] G. Zhang and Z. Song, Topological characterization of extended quantum Ising models, Phys. Rev. Lett. **115**, 177204 (2015).

[52] X.-G. Wen, Zoo of quantum-topological phases of matter, Rev. Mod. Phys. **89**, 041004 (2017).

[53] R. Verresen, N. G. Jones, and F. Pollmann, Colloquium: Topology and edge modes in quantum critical chains, Phys. Rev. Lett. **120**, 057001 (2018).

[54] Z. Gong, Y. Ashida, K. Kawabata, K. Takasan, S. Higashikawa, and M. Ueda, Topological phases of non-hermitian systems, Phys. Rev. X **8**, 031079 (2018).

[55] L. Pezzè, M. Gabbrielli, L. Lepori, and A. Smerzi, Multipartite entanglement in topological quantum phases, Phys. Rev. Lett. **119**, 250401 (2017).

[56] Y.-R. Zhang, Y. Zeng, H. Fan, J. Q. You, and F. Nori, Characterization of topological states via dual multipartite entanglement, Phys. Rev. Lett. **120**, 250501 (2018).

[57] Q.-Q. Wang, X.-Y. Xu, W.-W. Pan, S.-J. Tao, Z. Chen, Y.-T. Zhan, K. Sun, J.-S. Xu, G. Chen, Y.-J. Han, C.-F. Li, and G.-C. Guo, Robustness of entanglement as an indicator of topological phases in quantum walks, Optica **7**, 53 (2020).

[58] S. L. Braunstein and C. M. Caves, Statistical distance and the geometry of quantum states, Phys. Rev. Lett. **72**, 3439 (1994).

[59] V. Giovannetti, S. Lloyd, and L. Maccone, Quantum metrology, Phys. Rev. Lett. **96**, 010401 (2006).

[60] P. Hyllus, W. Laskowski, R. Krischek, C. Schwemmer, W. Wieczorek, H. Weinfurter, L. Pezzé, and A. Smerzi, Fisher information and multiparticle entanglement, Phys. Rev. A **85**, 022321 (2012).

[61] G. Tóth, Multipartite entanglement and high-precision metrology, Phys. Rev. A **85**, 022322 (2012).

[62] P. Hauke, M. Heyl, L. Tagliacozzo, and P. Zoller, Measuring multipartite entanglement through dynamic susceptibilities, Nat. Phys. **12**, 778 (2016).

[63] P. Laurell, A. Scheie, C. J. Mukherjee, M. M. Koza, M. Enderle, Z. Tylczynski, S. Okamoto, R. Coldea, D. A. Tennant, and G. Alvarez, Quantifying and controlling entanglement in the quantum magnet $Cs_2CoCl_4$, Phys. Rev. Lett. **127**, 037201 (2021).

[64] A. Scheie, P. Laurell, A. M. Samarakoon, B. Lake, S. E. Nagler, G. E. Granroth, S. Okamoto, G. Alvarez, and D. A. Tennant, Witnessing entanglement in quantum magnets using neutron scattering, Phys. Rev. B **103**, 224434 (2021).

[65] M. Cheneau, P. Barmettler, D. Poletti, M. Endres, P. Schauß, T. Fukuhara, C. Gross, I. Bloch, C. Kollath, and S. Kuhr, Light-cone-like spreading of correlations in aquantum many-body system, Nature (London) **481**, 484 (2012).

[66] P. Jurcevic, B. P. Lanyon, P. Hauke, C. Hempel, P. Zoller, R. Blatt, and C. F. Roos, Quasiparticle engineering and entanglement propagation in a quantum many-body system, Nature (London) **511**, 202 (2014).

[67] L. Bonnes, F. H. L. Essler, and A. M. Läuchli, "Light-cone" dynamics after quantum quenches in spin chains, Phys. Rev. Lett. **113**, 187203 (2014).
[68] Z. Yan, Y.-R. Zhang, M. Gong, Y. Wu, Y. Zheng, S. Li, C. Wang, F. Liang, J. Lin, Y. Xu, C. Guo, L. Sun, C.-Z. Peng, K. Xia, H. Deng, H. Rong, J. Q. You, F. Nori, H. Fan, X. Zhu *et al.*, Strongly correlated quantum walks with a 12-qubit superconducting processor, Science **364**, 753 (2019).
[69] E. Barouch, B. M. McCoy, and M. Dresden, Statistical mechanics of the *XY* model. I, Phys. Rev. A **2**, 1075 (1970).
[70] E. Barouch and B. M. McCoy, Statistical mechanics of the *XY* model. II. Spin-correlation functions, Phys. Rev. A **3**, 786 (1971).
[71] E. Lieb, T. Schultz, and D. Mattis, Two soluble models of an antiferromagnetic chain, Ann. Phys. **16**, 407 (1961).
[72] I. Titvinidze and G. I. Japaridze, Phase diagram of the spin S = 1/2 extended *XY* model, Eur. Phys. J. B **32**, 383 (2003).
[73] M. Fabrizio, Superconductivity from doping a spin-liquid insulator: A simple one-dimensional example, Phys. Rev. B **54**, 10054 (1996).
[74] R. Arita, K. Kuroki, H. Aoki, and M. Fabrizio, Density-matrix renormalization-group study of the spin gap in a one-dimensional Hubbard model: Effect of the distant transfer and exchange coupling, Phys. Rev. B **57**, 10324 (1998).
[75] S. Daul and R. M. Noack, Phase diagram of the half-filled Hubbard chain with next-nearest-neighbor hopping, Phys. Rev. B **61**, 1646 (2000).
[76] C. Aebischer, D. Baeriswyl, and R. M. Noack, Dielectric catastrophe at the mott transition, Phys. Rev. Lett. **86**, 468 (2001).
[77] O. Menchyshyn, V. Ohanyan, T. Verkholyak, T. Krokhmalskii, and O. Derzhko, Magnetism-driven ferroelectricity in spin-1/2 *XY* chains, Phys. Rev. B **92**, 184427 (2015).
[78] M. Hillery, Coherence as a resource in decision problems: The Deutsch-Jozsa algorithm and a variation, Phys. Rev. A **93**, 012111 (2016).
[79] H.-L. Shi, S.-Y. Liu, X.-H. Wang, W.-L. Yang, Z.-Y. Yang, and H. Fan, Coherence depletion in the Grover quantum search algorithm, Phys. Rev. A **95**, 032307 (2017).
[80] M. Horodecki and J. Oppenheim, Fundamental limitations for quantum and nanoscale thermodynamics, Nat. Commun. **4**, 2059 (2013).
[81] F. G. S. L. Brandão, M. Horodecki, J. Oppenheim, J. M. Renes, and R. W. Spekkens, Resource theory of quantum states out of thermal equilibrium, Phys. Rev. Lett. **111**, 250404 (2013).
[82] G. Gour, M. P. Müller, V. Narasimhachar, R. W. Spekkens, and N. Y. Halpern, The resource theory of informational nonequilibrium in thermodynamics, Phys. Rep. **583**, 1 (2015).
[83] H.-L. Shi, S. Ding, Q.-K. Wan, X.-H. Wang, and W.-L. Yang, Entanglement, coherence, and extractable work in quantum batteries, Phys. Rev. Lett. **129**, 130602 (2022).
[84] K. Życzkowski, P. Horodecki, M. Horodecki, and R. Horodecki, Dynamics of quantum entanglement, Phys. Rev. A **65**, 012101 (2001).
[85] S. Scheel, J. Eisert, P. L. Knight, and M. B. Plenio, Hot entanglement in a simple dynamical model, J. Mod. Opt. **50**, 881 (2003).
[86] T. Yu and J. H. Eberly, Finite-time disentanglement Via spontaneous emission, Phys. Rev. Lett. **93**, 140404 (2004).
[87] M. P. Almeida, F. de Melo, M. Hor-Meyll, A. Salles, S. P. Walborn, P. H. Souto Ribeiro, and L. Davidovich, Environment-induced sudden death of entanglement, Science **316**, 579 (2007).
[88] J. Laurat, K. S. Choi, H. Deng, C. W. Chou, and H. J. Kimble, Heralded entanglement between atomic ensembles: Preparation, decoherence, and scaling, Phys. Rev. Lett. **99**, 180504 (2007).
[89] T. Yu and J. H. Eberly, Sudden death of entanglement, Science **323**, 598 (2009).
[90] R. B. Sher and R. J. Daverman, *Handbook of Geometric Topology* (Elsevier, Amsterdam, 2002).
[91] T. R. Bromley, M. Cianciaruso, and G. Adesso, Frozen quantum coherence, Phys. Rev. Lett. **114**, 210401 (2015).
[92] X.-D. Yu, D.-J. Zhang, C. L. Liu, and D. M. Tong, Measure-independent freezing of quantum coherence, Phys. Rev. A **93**, 060303(R) (2016).
[93] M.-L. Hu and H. Fan, Evolution equation for quantum coherence, Sci. Rep. **6**, 29260 (2016).
[94] I. A. Silva, A. M. Souza, T. R. Bromley, M. Cianciaruso, R. Marx, R. S. Sarthour, I. S. Oliveira, R. Lo Franco, S. J. Glaser, E. R. de Azevedo, D. O. Soares-Pinto, and G. Adesso, Observation of time-invariant coherence in a nuclear magnetic resonance quantum simulator, Phys. Rev. Lett. **117**, 160402 (2016).
[95] K. Modi, T. Paterek, W. Son, V. Vedral, and M. Williamson, Unified view of quantum and classical correlations, Phys. Rev. Lett. **104**, 080501 (2010).
[96] A. Streltsov, G. Adesso, M. Piani, and D. Bruß, Are general quantum correlations monogamous, Phys. Rev. Lett. **109**, 050503 (2012).
[97] Y.-K. Bai, N. Zhang, M.-Y. Ye, and Z. D. Wang, Exploring multipartite quantum correlations with the square of quantum discord, Phys. Rev. A **88**, 012123 (2013).
[98] L. Mazzola, J. Piilo, and S. Maniscalco, Sudden transition between classical and quantum decoherence, Phys. Rev. Lett. **104**, 200401 (2010).
[99] B. You and L.-X. Cen, Necessary and sufficient conditions for the freezing phenomena of quantum discord under phase damping, Phys. Rev. A **86**, 012102 (2012).
[100] B. Dakić, Y. O. Lipp, X. Ma, M. Ringauer, S. Kropatschek, S. Barz, T. Paterek, V. Vedral, A. Zeilinger, Č. Brukner, and P. Walther, Quantum discord as resource for remote state preparation, Nat. Phys. **8**, 666 (2012).
[101] E. Chitambar, A. Streltsov, S. Rana, M. N. Bera, G. Adesso, and M. Lewenstein, Assisted distillation of quantum coherence, Phys. Rev. Lett. **116**, 070402 (2016).
[102] K.-D. Wu, Z. Hou, Y.-Y. Zhao, G.-Y. Xiang, C.-F. Li, G.-C. Guo, J. Ma, Q.-Y. He, J. Thompson, and M. Gu, Experimental cyclic interconversion between coherence and quantum correlations, Phys. Rev. Lett. **121**, 050401 (2018).
[103] V. Giovannetti, S. Lloyd, and L. Maccone, Advances in quantum metrology, Nat. Photon. **5**, 222 (2011).
[104] L. Pezzè, A. Smerzi, M. K. Oberthaler, R. Schmied, and P. Treutlein, Quantum metrology with nonclassical states of atomic ensembles, Rev. Mod. Phys. **90**, 035005 (2018).
[105] C. Portmann and R. Renner, Security in quantum cryptography, Rev. Mod. Phys. **94**, 025008 (2022).

[106] Y. K. Wang, Y. R. Zhang, and H. Fan, One-way deficit and quantum phase transitions in *XY* model and extended Ising model, Quantum Inf. Process. **18**, 19 (2019).

[107] Q. Chen, C. Zhang, S. Yu, X. X. Yi, and C. H. Oh, Quantum discord of two-qubit *X* states, Phys. Rev. A **84**, 042313 (2011).

[108] M. S. Sarandy, Classical correlation and quantum discord in critical systems, Phys. Rev. A **80**, 022108 (2009).